1
2
3
4
5
6
7
8
9
10
11
12
13
14
15
16
17
18
19
20
21
22
23
24
25
26
27
28
29
30
31
32
33
34
35
36
37
38
39
40
41
42
43
44
45
46
47
48
49
50
51
52
53
54
55
56
57
58
59
60
61
62
63
64
65

A SPH Solver for Simulating Paramagnetic Solid-Fluid Interaction in the Presence of an External Magnetic Field

M.R. Hashemi[a], M.T. Manzari[a,*], R. Fatehi[b]

[a]*Center of Excellence in Energy Conversion, School of Mechanical Engineering, Sharif University of Technology, Tehran, Iran.*
[b]*Department of Mechanical Engineering, Persian Gulf University, Bushehr 75169, Iran.*

*Corresponding author. Tel: +98 21 6616 5689; Fax: +98 21 6600 0021
Email address: mtmanzari@sharif.edu (M.T. Manzari)

A SPH Solver for Simulating Paramagnetic Solid-Fluid Interaction in the Presence of an External Magnetic Field

Abstract

The Smoothed Particle Hydrodynamics (SPH) method is extended to solve magnetostatic problems involving magnetically interacting solid bodies. In order to deal with the jump in the magnetic permeability at a fluid-solid interface, a consistent SPH scheme is utilized and a modified formulation is proposed to calculate the magnetic force density along the interface. The results of the magnetostatic solver are verified against those of the finite element method. The governing fluid flow equations are discretized using the same SPH scheme, developing an efficient method for simulating the motion of paramagnetic solid bodies in a fluid flow. The proposed algorithm is applied to a benchmark problem including a suspended paramagnetic solid body moving under the influence of a non-uniform magnetic field and the result is validated against literature. The proposed method is further verified by simulating the magneto-hydrodynamic interaction of two suspended circular cylinders. As a more complex test-case, the evolution of a suspended magnetic chain under the influence of a rotating magnetic field is also simulated. The deformation of a chain formed by a number of paramagnetic solid bodies in a shear flow is simulated. Steady state and dynamic responses of the magnetic chain are investigated under steady and oscillatory shear flows. The effects of Reynolds number, solid volume fraction, strength of the external magnetic field and the number of solid bodies forming the chain, are discussed.

Keywords:
Smoothed Particle Hydrodynamics (SPH), Magnetorheology, Magnetostatics, Particulate Flow

1. Introduction

Using the influence of a controlled magnetic field on (para-)magnetic solid particles suspended in a non-magnetic fluid is a brand new technique in various applications [1, 2, 3]. In biomedicine, this technique can help in active drug delivery [4], cell separation [4, 2] or mixing [5]. Active control of the rheology of a magnetorheological fluid is also possible under the influence of a controlled magnetic field [6]. In a magnetorheological fluid, magnetic chains are formed using suspended solid particles and can result in an increase in the flow resistance [7].

Studying a magnetorheological fluid under shear reveals valuable rheological properties [8] which are essential in various applications; *e.g.* viscosity as a function of the external magnetic field. These properties are mainly determined by the strength of the linking force between solid particles and the consequent deformations of magnetic chains. Therefore, investigating the mechanisms

2

of the migration of magnetic solid particles and the micro-structures formed by these particles is needed. In the past decade, theories have been developed to correlate the shear behaviour of magnetorheological fluids with structural deformation of the chains formed by magnetic particles. de Vicente *et al.* [9] described the shear stress as a function of the Mason number, which is a non-dimensional parameter defined as the ratio of the viscous force to the magnetic force. In recent years, due to practical limitations in experimental studies, numerical simulation has become a viable alternative to experiment.

Several numerical methods based on Brownian dynamics, have been developed to investigate the structure of magnetic chains in a magnetorheological fluid [10, 11, 12]. In these methods, hydrodynamic interactions are neglected and a dipole-dipole model mimics the magnetic effects. Although neglecting hydrodynamic interactions gives a reasonable measure of the bulk properties of a magnetorheological fluid, the micro-structures can be accurately studied only by including the hydrodynamic interactions [13]. To alleviate this problem, the Stokesian dynamics [14, 15] has been used to replace a simple drag force with a more accurate approximation of the hydrodynamic inter-actions [13]. However, this method is limited to the Stokes flow regime and there is no systematic approach to implement complex boundaries. A similar technique was developed by Gao *et al.* [16] and was utilized to simulated the evolution of a magnetic chain under the influence of a rotating magnetic field.

Another key issue is an accurate calculation of the magnetic interaction between solid particles in a magnetorheological fluid. When two magnetic beads of finite size are approaching each other the magnetic interaction could no longer be represented by a simple dipole-dipole model [17]. In order to overcome this shortcoming, either a finite-dipole model [17] is used or the magnetostatic problem is solved using a numerical technique [18]. In 2011, Suh and Kang [19] provided a semi-analytical solution for multiple interacting paramagnetic particles.

An accurate description of the micro-structures in a magnetorheological fluid, can only be pro-vided using a Direct Numerical Simulation (DNS) [20]. In this approach, the governing equations of the fluid flow and the magnetic problem are numerically solved. This leads to a more accurate calculation of the hydrodynamic and magnetic interactions in comparison with the previously dis-cussed methods [21, 22]. In 2008, Kang *et al.* [21] proposed a Finite Element Method (FEM) in which the moving solid bodies are modelled using a fictitious domain technique. This method has been successfully used in the studies regarding the deformation of a magnetic chain in a micro-mixer under the influence of a rotating magnetic field [1]. In 2012, Kang *et al.* [23] investigated the shear behaviour of magnetic chains using the same DNS approach in two-dimensions. They reported the apparent viscosity of the system as a function of Mason number based on observations for specific test-cases. Another method was proposed by Kang and Suh [22] in which, the magnetic permeability was smoothly distributed and an immersed boundary finite volume method was used as a hydrodynamic solver.

The above mentioned DNS approaches are based on Eulerian grid-based methods. In these methods, additional effort is needed to model a moving solid boundary and track a suspended solid body in the flow. On the other hand, the mesh-free nature and the Lagrangian formulation of the Smoothed Particle Hydrodynamics (SPH) method make it a suitable approach in particulate flow simulations [24, 25]. The main goal of this paper is to develop a SPH method for direct simulation of paramagnetic solid bodies suspended in a Newtonian fluid under the influence of an external magnetic field. To this end, it is needed to solve the governing equations of the magnetic problem as well as the hydrodynamics associated with the moving solid bodies.

In order to solve the magnetic problem with a jump in the magnetic permeability on the fluid-

3

solid interface, using the conventional methods, either a boundary fitted mesh is needed or rich elements with auxiliary nodes are required [26]. In the present method, however, the fluid-solid interface is represented by a layer of SPH particles [25]. Since in the SPH method, equations are solved in their strong form, the discontinuity of the magnetic permeability can be handled only by directly imposing the continuity of magnetic flux as a boundary condition on fluid-solid interfaces. This leads to difficulties in the calculation of the magnetic force using the standard form of the Maxwell stress tensor as described in [27]. Therefore, in the present method, magnetic forces are calculated using a modified formulation similar to that introduced in [19].

It must be noted that, the implementation of the magnetic flux conservation on a fluid-solid interface is possible only within the framework of a consistent SPH scheme [28]. To the best of authors' knowledge, this is the first time that SPH is used in the calculation of the magnetic interaction between solid bodies. In this sense, the SPH method is considered as a substitute for the conventional methods used in magnetostatic problems.

In the hydrodynamic solver, the equations governing the Newtonian fluid flow are discretized using the same consistent SPH scheme as the magnetostatic solver. In order to stabilize the SPH method, a corrected continuity equation and a modified particle shifting technique [29] are utilized. A consistent and efficient implementation for the moving solid boundary is also used [25]. The proposed magnetostatic solver is coupled with the hydrodynamic solver through the Newton's law governing the motion of paramagnetic solid bodies. It must be noted that, unlike previous methods [21, 22], here inertia which plays an important role in dynamic tests is present.

In the following, first the governing equations and their implementation within the framework of a consistent SPH method are described. The performance of the magnetostatic solver is analysed and the results are compared with those of the Finite Element Method (FEM). The coupled magnetostatic-hydrodynamic solver is then benchmarked against the FEM results reported in [21] for a suspended paramagnetic solid body under the influence of an external non-uniform magnetic field. The magneto-hydrodynamic interaction of two paramagnetic solid bodies under the influence of a constant external magnetic field is simulated and the result is verified against literature [22]. The proposed method is then applied to the evolution of a chain of paramagnetic solid bodies under the influence of a rotating external magnetic field which possibly involves a chain rupture [1]. A periodic array of chains formed by paramagnetic circular solid bodies under the influence of an external magnetic field, is simulated in a confined shear flow. The configuration of the magnetic chain and the apparent viscosity of the system are investigated as functions of the solid volume fraction and the intensity of the external magnetic field. The response of the system to a Small Amplitude Oscillatory Shear (SAOS) is studied and the viscoelastic behaviour of the system [30] is qualitatively discussed.

2. Governing Equations

The main goal of this paper is to introduce a computational algorithm for simulating the motion of paramagnetic solid bodies suspended in a Newtonian fluid. Therefore, the partial differential equations governing the hydrodynamic and magnetic problems should be solved sequentially to calculate the hydrodynamic and magnetic interactions, respectively.

4

2.1. Hydrodynamics

The laminar Newtonian fluid flow in a Lagrangian framework is governed by momentum conservation

$$\rho \frac{d\mathbf{v}}{dt} = -\nabla p + \eta \nabla^2 \mathbf{v}, \tag{1}$$

and the mass balance equation

$$\frac{d\rho}{dt} = -\rho \nabla \cdot \mathbf{v}. \tag{2}$$

In these equations, $\mathbf{v}$ is the velocity vector, ρ is density, p is the pressure field and the dynamic viscosity is η. Here, fluid is considered to be weakly compressible [31] and pressure field is calculated using an equation of state as

$$p - p_0 = c_0^2 (\rho - \rho_0), \tag{3}$$

where the subscript 0 denotes the initial state. It must be noted that, the artificial speed of sound, c_0, is chosen in a way that the fluid does not deviate from its incompressible nature, or equivalently the Mach number in the flow domain should remain less than 0.1 [31]. However, at a very low Reynolds numbers a Mach number of the order of 10^{-2} [32] or even less [24] may be required.

On a solid wall, the no-slip condition is imposed and pressure is calculated using the following boundary condition [25]

$$\frac{\nabla p}{\rho} \cdot \mathbf{n} = \left(-\frac{d\mathbf{v}}{dt} + \frac{\nabla \cdot \boldsymbol{\tau}}{\rho} \right) \cdot \mathbf{n}, \tag{4}$$

where $\mathbf{n}$ is a unit vector normal to the surface and $\boldsymbol{\tau}$ is the viscous stress tensor.

2.2. Magnetostatics

In most applications, *e.g.* magnetorheological fluids, changes in the configuration of the magnetic particles happen in a time-scale much larger than the electromagnetic time-scale [18]. Therefore, magnetic field in the absence of free current, is considered to be governed by the magnetostatic Maxwell's equations [27, 33]

$$\nabla \times \mathbf{H} = 0, \tag{5}$$

written for the magnetic field intensity, $\mathbf{H}$, and

$$\nabla \cdot \mathbf{B} = 0, \tag{6}$$

for the magnetic flux density, $\mathbf{B}$. The relation between $\mathbf{B}$ and $\mathbf{H}$ is described using a constitutive equation as [27]

$$\mathbf{B} = \mu \mathbf{H}. \tag{7}$$

In the present work, the magnetic permeability, μ, is considered to be constant for an isotropic paramagnetic material far below the magnetic saturation limit [34]. At an interface which specifies a jump in the material properties 1 and 2, Maxwell's equations are subjected to boundary conditions [27]

$$\mathbf{n} \cdot (\mathbf{B}_2 - \mathbf{B}_1) = 0, \tag{8}$$

which states that the normal component of $\mathbf{B}$ is constant across a surface, and

$$\mathbf{n} \times (\mathbf{H}_2 - \mathbf{H}_1) = 0, \tag{9}$$

5

which denotes that the tangential component of $\mathbf{H}$ is constant across the interface. Here, $\mathbf{n}$ is a unit vector normal to the interface drawn from 1 to 2.

The fact that in the absence of free current magnetic field is irrotational (see Eq. (5)) implies that the magnetic field can be represented utilizing a scalar potential, ϕ, as [27, 18]

$$\mathbf{H} = \nabla\phi. \tag{10}$$

Therefore, using Eq. (6), one obtains

$$\nabla \cdot (\mu\nabla\phi) = 0. \tag{11}$$

In order to solve the Laplace equation (11), the boundary conditions (8) and (9) are needed to be rewritten in terms of ϕ. It can be shown that the required boundary conditions at the interface are [18]

$$\phi_1 - \phi_2 = 0, \tag{12}$$

and

$$\mu_1\mathbf{n} \cdot \nabla\phi_1 - \mu_2\mathbf{n} \cdot \nabla\phi_2 = 0. \tag{13}$$

Equation (11) along with boundary conditions (12) and (13) lead to a linear system of equations for ϕ. Using Eqs. (10) and (7), the magnetic flux density is calculated. In order to obtain the magnetic force, the Maxwell stress tensor is introduced as [33]

$$\mathbf{T_m} = \frac{1}{\mu}\left(\mathbf{BB} - \frac{1}{2}\mathbf{B} \cdot \mathbf{B}\boldsymbol{\delta}\right), \tag{14}$$

where $\boldsymbol{\delta}$ is the identity tensor. In this way, the magnetic force density, $\mathbf{f}_m$, is calculated as

$$\mathbf{f}_m = \nabla \cdot \mathbf{T_m}. \tag{15}$$

In the absence of a free current, $\mathbf{f}_m$ can also be represented in a manipulated form as [19]

$$\mathbf{f}_m = -\frac{1}{2}\mathbf{H} \cdot \mathbf{H}\nabla\mu. \tag{16}$$

Therefore, magnetic force only acts on the fluid-solid interfaces with a jump in the magnetic permeability and tends to zero within homogeneous domains [21].

3. Smoothed Particle Hydrodynamics

In the SPH method, the computational domain is discretized using particles in a Lagrangian framework. Interpolations are conducted using a summation with a weighting function, W, called *kernel* as

$$\langle A\left(\mathbf{r}\right)\rangle = \sum_{\mathrm{j}} \frac{m_{\mathrm{j}}}{\rho_{\mathrm{j}}} A_{\mathrm{j}} W\left(|\mathbf{r} - \mathbf{r}_{\mathrm{j}}|, h\right), \tag{17}$$

where A is any field variable, j denotes the neighbouring particles positioned within the circle of the compact support of the kernel function with its center positioned at $\mathbf{r}$, and m_{j} and ρ_{j} are mass and density of particle j, respectively. Kernel represents Dirac delta function with the cut-off distance of h [35]. In this work, the quintic Wendland function is used as the kernel of SPH with $h/\delta_p = 2.6$, where δ_p is the initial particle spacing.

The first order renormalized spatial derivative scheme as introduced in [36] is

$$\langle \nabla A \rangle_i = \sum_j \frac{m_j}{\rho_j} \mathbf{C}_i \cdot \boldsymbol{e}_{ij} W'_{ij} A_{ij}, \tag{18}$$

where, C is the renormalization tensor

$$\mathbf{C}_i = - \left[\sum_j \frac{m_j}{\rho_j} r_{ij} \boldsymbol{e}_{ij} \boldsymbol{e}_{ij} W'_{ij} \right]^{-1}. \tag{19}$$

It is shown that such a renormalization compensates for incompleteness of support domain [28] especially in the vicinity of a boundary [29]. In a similar way, the renormalized second order spatial derivative scheme was introduced by Fatehi and Manzari [28] as

$$\langle \nabla^2 A \rangle_i = \hat{\mathbf{C}}_i : \sum_j 2 \frac{m_j}{\rho_j} \mathbf{e}_{ij} \mathbf{e}_{ij} W'_{ij} \left(\frac{A_{ij}}{r_{ij}} - \langle \mathbf{e}_{ij} \cdot \nabla A \rangle_i \right). \tag{20}$$

In the above equations, $A_{ij} = A_j - A_i$, $W'_{ij} = \frac{\partial W(|\mathbf{r} - \mathbf{r}_j|, h)}{\partial r} |_{\mathbf{r} = \mathbf{r}_i}$, $\mathbf{r}_{ij} = \mathbf{r}_i - \mathbf{r}_j$, $r = |\mathbf{r}|$, and $\boldsymbol{e}_{ij}$ is the unit vector pointing from neighbouring particle j towards i. The renormalization tensor $\hat{\mathbf{C}}$ is obtained from the following set of equations

$$\hat{\mathbf{C}}_i : \mathbf{D}_i = -\boldsymbol{\delta}, \tag{21}$$

where

$$\mathbf{D}_i = \sum_j \frac{m_j}{\rho_j} r_{ij} \mathbf{e}_{ij} \mathbf{e}_{ij} \mathbf{e}_{ij} \mathbf{e}_{ij} W'_{ij} + \left(\sum_j \frac{m_j}{\rho_j} \mathbf{e}_{ij} \mathbf{e}_{ij} \mathbf{e}_{ij} W'_{ij} \right) \cdot \mathbf{C}_i \cdot \left(\sum_j \frac{m_j}{\rho_j} r_{ij}^2 \mathbf{e}_{ij} \mathbf{e}_{ij} \mathbf{e}_{ij} W'_{ij} \right). \tag{22}$$

In two-dimensions, Eq. (21) is reduced to a system of three equations with three unknowns as

$$\begin{Bmatrix} D^{1111} & 2D^{2111} & D^{2211} \\ D^{1112} & 2D^{2112} & D^{2212} \\ D^{1122} & 2D^{2122} & D^{2222} \end{Bmatrix}_i \begin{Bmatrix} \hat{C}^{11} \\ \hat{C}^{12} \\ \hat{C}^{22} \end{Bmatrix}_i = \begin{Bmatrix} -1 \\ 0 \\ -1 \end{Bmatrix}, \tag{23}$$

where $\hat{C}_i^{\alpha\beta}$ and $D_i^{\alpha\beta\gamma\lambda}$ are components of $\hat{\mathbf{C}}_i$ and $\mathbf{D}_i$, respectively. It must be noted that $\hat{\mathbf{C}}$ is a symmetric tensor, *i.e.* $\hat{C}_i^{12} = \hat{C}_i^{21}$.

3.1. Implementation

From the viewpoint of computational costs it is more favourable to compute and store the spatial derivative operators (18) and (20), prior to solving the magnetostatic problem at each time step. To this end, variables $\mathbf{Z}$ and $\hat{Z}$ are defined as

$$\mathbf{Z}_{ij} = \frac{m_j}{\rho_j} \mathbf{C}_i \cdot \boldsymbol{e}_{ij} W'_{ij}, \tag{24}$$

and

$$\hat{Z}_{ij} = 2\frac{m_j}{\rho_j}\hat{\mathbf{C}}_i : \mathbf{e}_{ij}\mathbf{e}_{ij}W'_{ij}. \tag{25}$$

Therefore, the first order and the second order spatial derivative operators can be rewritten as

$$\langle \nabla A \rangle_i = \sum_j \mathbf{Z}_{ij}(A_j - A_i), \tag{26}$$

and

$$\langle \nabla^2 A \rangle_i = \sum_j \left[\frac{\hat{Z}_{ij}}{r_{ij}} - \left(\sum_k \hat{Z}_{ik}\mathbf{e}_{ik} \right) \cdot \mathbf{Z}_{ij} \right] (A_j - A_i), \tag{27}$$

respectively.

3.2. Moving Solid Bodies

The linear velocity $\mathbf{v}$ and the angular velocity $\mathbf{\Omega}$ of each solid body are governed by the Newton's law of motion as

$$M_s \frac{d\mathbf{v}_s}{dt} = \mathbf{F}_s^m + \mathbf{F}_s^h + \mathbf{F}_s^r \tag{28}$$

and

$$I_s \frac{d\mathbf{\Omega}_s}{dt} = \mathbf{M}_s^m + \mathbf{M}_s^h \tag{29}$$

where M_s and I_s are the total mass and moment of inertia of solid body s, respectively. The right-hand side of Eq. (28) gives the net force acting on a solid body consisting of the magnetic force, $\mathbf{F}^m$, the hydrodynamic interaction, $\mathbf{F}^h$, and the repulsive force due to solid-solid collisions, $\mathbf{F}^r$. In a similar way, the right-hand side of Eq. (29) is the net moment including the magnetic and hydrodynamic effects. In this paper, Brownian motions and the moment due to solid-solid collisions are neglected. However, it is straightforward to add the Brownian effects in the SPH method [24].

The hydrodynamic force $\mathbf{F}_s^h$ and moment $\mathbf{M}_s^h$ are calculated as

$$\mathbf{F}_s^h = \sum_j \left(-p_j\mathbf{n}_j + \mathbf{n}_j \cdot \boldsymbol{\tau}_j\right)\Delta S_j, \tag{30}$$

and

$$\mathbf{M}_s^h = \sum_j \boldsymbol{\rho}_j^s \times \left(-p_j\mathbf{n}_j + \mathbf{n}_j \cdot \boldsymbol{\tau}_j\right)\Delta S_j, \tag{31}$$

respectively. Here, j denotes the SPH particles positioned on the boundary of solid body s, $\mathbf{n}$ is the unit outward normal vector and vector $\boldsymbol{\rho}_j^s$ points to j from the center of mass of s. The boundary segment, ΔS, denotes the portion of the solid surface associated with a SPH boundary particle.

In the present method, a simple short-range repulsive force is considered to prevent the interference of the magnetically interacting circular solid bodies as

$$\mathbf{F}_{sq}^r = F_0\exp\left(k_1\frac{k_2h_c - h}{a_s + a_q}\right)\mathbf{e}_{sq} \tag{32}$$

where q and s denote two interacting solid bodies, h is gap between solid surfaces, a is radius, and $\mathbf{e}_{sq} = \frac{\mathbf{r}_s - \mathbf{r}_q}{|\mathbf{r}_s - \mathbf{r}_q|}$. This repulsive force is active when $h \leq h_c$ and h_c is in the order of SPH particle
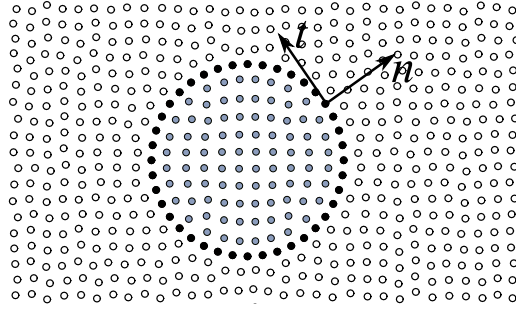
Figure 1: SPH particles distribution around a suspended solid body. White circles represent SPH particles in the fluid domain, dark ones represent the solid boundary, and SPH particles inside solid body which participate in the magnetostatic problem are shaded (gray).

spacing (in this work, $h_c = \delta_p$). Coefficient F_0 defines the magnitude of the repulsive force, and constants k_1 and k_2 are tuning parameters set to $k_1 = 20$ and $k_2 = 0.5$. Total repulsive force acting on solid body s is calculated using a summation over all neighbouring solid bodies colliding with s, i.e. $\mathbf{F}_s^r = \sum_q \mathbf{F}_{sq}^r$. The repulsive force should act as a stiff spring between solid bodies [37]. However, in order to balance the magnetic attraction, the repulsive force has a positive value at the onset of collision, i.e. $|\mathbf{F}^r||_{h=h_c} > 0$. It must be noted that in order to improve the accuracy, other more complex collision strategies (see [37] for example) can be implemented which most of the time require higher computational costs.

3.3. Magnetic Force

Figure 1 presents the arrangement of SPH particles around a solid body. As seen in this figure, the interior of the solid body is filled with SPH particles. These SPH particles are linked to the corresponding boundary particles and the whole set moves as a rigid body. These SPH particles facilitate solving the magnetostatic problem, and except for those positioned on a solid boundary, have no role in the hydrodynamic problem. In this way, since there is only one layer of SPH particles defining the interface, the magnetic potential is continuous and boundary condition (12) is automatically satisfied. Equation (11) along with boundary condition (13) are discretized using the spatial derivative operators (26) and (27). It must be noted that, the effect of the external magnetic flux density, $\mathbf{B}_0$, is considered by imposing the scalar potential ϕ_0 as a Dirichlet boundary condition on the external boundaries of the whole domain, in a way that $\mathbf{B}_0 = \mu_f \nabla \phi_0$, where subscript f denotes the fluid domain [21, 22]. The resulting system of linear equations is solved using the stabilized bi-conjugate gradient method provided in an open-source C++ package (Seldon) [38] with a diagonal pre-conditioner.

In conventional grid-based methods, as in the finite element method, the net magnetic force acting on a solid body is calculated by integrating the magnetic force density (15) on the area (volume in 3D) of the suspended solid body [21]. However, in the present work, integrating (15) on the SPH particles confined within boundaries of a solid body does not give a correct approximation of the magnetic force. In order to resolve this issue, Eq. (16) is integrated across the interface in a similar way as proposed in [19] for a semi-analytical method. In Appendix **I**, it is shown that the

9

magnetic force density per unit length (area in 3D) of the interface between materials 1 and 2 is

$$\hat{\mathbf{f}}^m = \frac{1}{2}\left[\left(\frac{1}{\mu_s} - \frac{1}{\mu_f}\right)(\mu\mathbf{n}\cdot\nabla\phi)^2 - (\mu_s - \mu_f)(\mathbf{t}\cdot\nabla\phi)^2\right], \tag{33}$$

where subscripts s and f denote the quantities corresponding to the solid and the fluid domains, respectively. It must be noted that, $(\mu\mathbf{n}\cdot\nabla\phi)_s = (\mu\mathbf{n}\cdot\nabla\phi)_f$ and $(\mathbf{t}\cdot\nabla\phi)_s = (\mathbf{t}\cdot\nabla\phi)_f$. Similar to Eqs. (30) and (31), total magnetic force and moment acting on solid body s are obtained by integrating $\hat{\mathbf{f}}^m$ on its boundary as

$$\mathbf{F}_s^m = \sum_j \hat{\mathbf{f}}_j^m \Delta S_j, \tag{34}$$

and

$$\mathbf{M}_s^m = \sum_j \boldsymbol{\rho}_j^s \times \hat{\mathbf{f}}_j^m \Delta S_j, \tag{35}$$

respectively.

3.4. Stabilized SPH Method

3.4.1. Modified Continuity Equation

In order to resolve the instabilities associated with spurious pressure oscillations, Eq. (2) is replaced by a modified continuity equation proposed in [29]

$$\frac{d\rho}{dt} = -\rho\left[\nabla\cdot\mathbf{v} + \Delta t\left(\left\langle\nabla\cdot\left\langle\frac{\nabla p}{\rho}\right\rangle\right\rangle - \left\langle\nabla\cdot\frac{\nabla p}{\rho}\right\rangle\right)\right], \tag{36}$$

where Δt is the time-step size. Additional terms in the RHS of (36) are discretized using the renormalized spatial derivative schemes as

$$\left\langle\nabla\cdot\left\langle\frac{\nabla p}{\rho}\right\rangle\right\rangle_\mathrm{i} = \sum_\mathrm{j} \mathbf{Z}_\mathrm{ij}\cdot\left(\left\langle\frac{\nabla p}{\rho}\right\rangle_\mathrm{j} - \left\langle\frac{\nabla p}{\rho}\right\rangle_\mathrm{i}\right), \tag{37}$$

and

$$\left\langle\nabla\cdot\frac{\nabla p}{\rho}\right\rangle_\mathrm{i} = \sum_\mathrm{j} \bar{Z}_\mathrm{ij}\left(\frac{p_\mathrm{i}-p_\mathrm{j}}{\bar{\rho}_\mathrm{ij}r_\mathrm{ij}} - \left\langle\mathbf{e}_\mathrm{ij}\cdot\frac{\nabla p}{\rho}\right\rangle_\mathrm{i}\right), \tag{38}$$

where $\bar{\rho}_\mathrm{ij} = (\rho_\mathrm{i} + \rho_\mathrm{j})/2$. In this way, Eq. (36) approaches to the standard formulation (2) as $\delta_p \to 0$ [29].

3.4.2. SPH Particle Shifting

Particle shifting proposed by Xu *et al.* [39] is a remedy to the SPH particle clustering. However in this work, a modified shifting technique introduced in [29], is found to be more convenient for solid bodies which are nearly in contact. In this method, SPH particle i positioned within a fluid domain at $\mathbf{r}_i$, is moved at the end of each time step according to

$$\mathbf{r}_i^{new} = \mathbf{r}_i + \epsilon\sum_j \frac{1}{\psi_j}\mathbf{r}_{ij}W_{ij}, \tag{39}$$

10

where j denotes the neighbouring SPH particles, $\epsilon = 0.03$ and $\psi_i = \sum_j W_{ij}$ is the particle number density. In order to keep the accuracy of the results, field variables are updated at the end of shifting procedure using the Taylor series expansion as described in [39]. Using this technique, SPH particles are arranged around a solid surface defined by one layer of SPH particles, at a distance slightly larger than δ_p.

3.5. Remarks

The magnetostatic problem and the fluid flow are coupled via changes in the fluid-solid interfaces occur due to the movement of the suspended solid bodies. Therefore, one should solve the magneto-static problem once the configuration of the solid bodies changes. In this work, a predictor-corrector scheme presented in Appendix **II** is used for the hydrodynamic problem while the magnetic forces are calculated just at the beginning of each time-step.

It must be noted that the renormalized first spatial derivative scheme (26) is used for the pressure gradient, and the Laplacian of the velocity field is calculated using Eq. (27) as appeared in the momentum equation (1). Time derivative of the field variables is calculated using a first order discretization with a time-step, Δt, subjected to the following criteria

$$\Delta t = \min \left\{ \frac{0.65\delta_p}{c_0}, \frac{\rho(0.65\delta_p)^2}{\eta} \right\} \tag{40}$$

4. Results

4.1. Magnetic Force Verification

In this section, the proposed SPH method is verified for a magnetostatic problem involving the magnetic interaction of two circular cylinders. Fluid-solid interactions are neglected and a quantitative comparison of magnetic force is made with finite element solutions obtained using the FEMM package [40]. The problem is to calculate the magnetic interaction between two circular solid bodies of radius $a = 0.00125(m)$ positioned at $(r_0\cos\theta_0, r_0\sin\theta_0)$ and $(-r_0\cos\theta_0, -r_0\sin\theta_0)$ under the influence of the external magnetic field $\mathbf{B}_0$ applied in the x-direction. Magnetic solid bodies are confined in a circular cavity $(R = 0.01(m))$ filled with non-magnetic fluid f. A schematic of the problem is illustrated in Fig. 2. Solid bodies are considered to be of the same magnetic permeability μ_s.

Figure 3 presents the absolute error in the magnetic force, $Error = \frac{|\mathbf{F}^m_{SPH} - \mathbf{F}^m_{FEM}|}{|\mathbf{F}^m_{FEM}|}$, as a function of a/δ_p. Results were obtained for $r_0 = 0.00175(m)$, $\theta_0 = 0$ and $B_0 = |\mathbf{B}_0| = 1(T)$. T stands for Tesla, the unit of magnetic flux density. The magnetic susceptibility of circular solid bodies is $\chi = \frac{\mu_s - \mu_f}{\mu_f} = 0.1$. It is seen in Fig. 3, that the SPH results converge to the FEM solution. In the following, unless otherwise mentioned, $a/\delta_p = 18.75$ is used in the simulations.

A similar problem is solved to investigate the effects of magnetic susceptibility on the solution. Table 1 shows the results obtained for different values of χ and $B_0 = 100(T)$. In Fig. 4, $Error$ is presented as a function of χ. By increasing χ the growing discontinuity in the magnetic permeability leads to a sharper jump in the magnetic field normal to the fluid-solid interface (see Fig. 5). This in turn, results in higher errors in numerical simulations. However, for a very small magnetic susceptibility $(\chi < 0.1)$ the numerical truncation error becomes dominant.
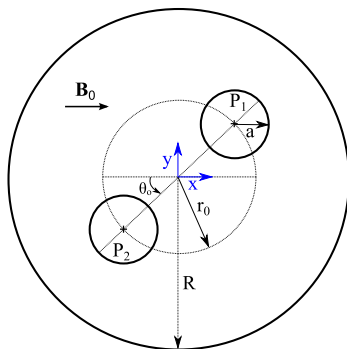
11

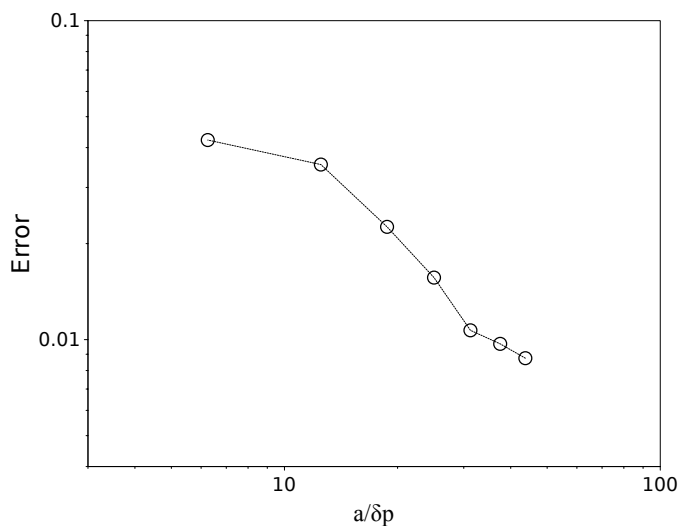Figure 2: Schematic of the magnetostatic problem.

Figure 3: Convergence of the megnetic force for $r_0 = 0.00175(m)$, $\theta_0 = 0$ and $B_0 = 1(T)$. *Error* as a function of a/δ_p.

Table 1: Magnetic force in the x-dirextion obtained for $B_0 = 100(T)$, $r_0 = 0.00175(m)$, $\theta_0 = 0$ and different values of χ.

χ	$F_x(N)$, SPH	$F_x(N)$, FEM	Error (%)
0.01	1.861×10^{-4}	1.788×10^{-4}	4.1
0.1	1.694×10^{-2}	1.660×10^{-2}	2.0
1.0	9.251×10^{-1}	8.933×10^{-1}	3.6
2.0	2.227	2.128	4.7
4.0	4.244	4.010	5.8
8.0	6.472	6.060	6.8

12

Figure 4: *Error* as a function of χ for $r_0 = 0.00175(m)$ and $\theta_0 = 0$.

(a)

(b)

Figure 5: Contours of the magnetic potential obtained for (a) $\chi = 1.0$ and (b) $\chi = 9.0$, with $r_0 = 0.00175(m)$ and $\theta_0 = 0$.

13

Figure 6: Magnetic force as a function of *Gap* between solid bodies in the (a) x-direction and (b) y-direction in comparison with FEM for $\theta_0 = 20°$.

Figure 6 presents the magnetic force as a function of $Gap = r_0 - a$, for $\theta_0 = 20°$ and $\chi = 0.1$. For this configuration, solid bodies are attracted to each other while the attraction force is (exponentially) decreasing with *Gap*. When solid bodies come to a near contact, *Error* slightly increases due to insufficient numerical resolution between the approaching solid surfaces. However, the maximum *Error* remains within 4%.

Using the standard SPH formulation, the results hardly converge by decreasing the particle spacing, while keeping the ratio of the smoothing length of the kernel function, h/δ_p, constant [28]. However, as previously discussed, the renormalized spatial derivative schemes resulted in convergent solutions with a relatively smaller h/δ_p. In Fig. 7, *Error* is shown as a function of h/δ_p for $r_0 = 0.00175(m)$ and $\theta_0 = 0$ with $\chi = 0.1$. It is observed that *Error* is slightly decreased by increasing the smoothing length of the SPH kernel function for $h/\delta_p > 2.5$. On the other hand, the computational cost increases by increasing h/δ_p due to a dramatic increase in the number of neighbouring SPH particles positioned within a kernel compact support. In this work, $h/\delta_p = 2.6$ is used as a compromise between the computational costs and *Error*. It must be noted that here, h refers to the kernel cut-off distance, and for $h/\delta_p = 2.6$, the kernel support encloses almost 21 SPH particles while this number is about 40 for $h/\delta_p = 3.5$. Also, a very large value of $h/\delta_p \geq 4$ smooths out the effects of the jump in the magnetic permeability at the fluid-solid interface, and therefore adds to the numerical error.

4.2. Test Problems

In Section 4.1, the performance of the magnetostatic solver was assessed in a static situation where the hydrodynamic forces acting on the solid bodies are absent. Here, the present method is used to solve benchmark problems in which both magnetic and hydrodynamic effects are present.

4.2.1. A Single Solid Body in a Closed Cavity

The first benchmark problem as previously solved in [21], deals with the motion of a (para)magnetic circular solid body under the influence of the magnetic field induced around a wire carrying electric current I. The solid body is neutrally buoyant and suspended in a Newtonian fluid confined in
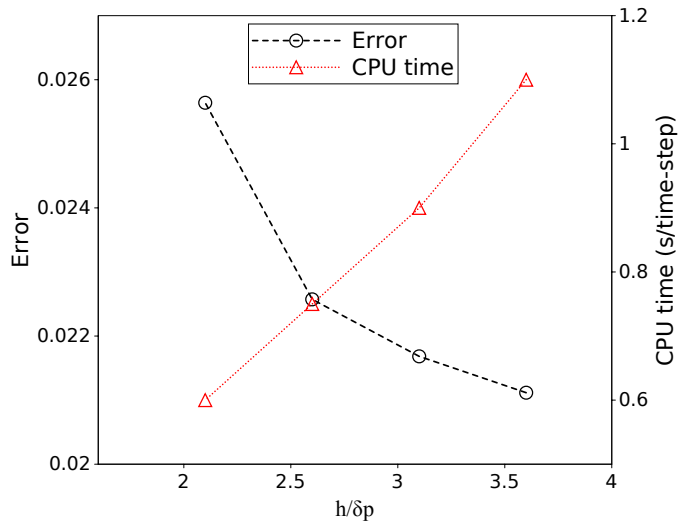
14

Figure 7: *Error* as a function of h/δ_p for $r_0 = 0.00175(m)$ and $\theta_0 = 0$ with $\chi = 0.1$.

a square cavity as schematically illustrated in Fig. 8. The suspending fluid is considered to be non-magnetic and the magnetic susceptibility of the solid body is $\chi = 1$. The system is initially at rest and the fluid flows at a vanishing Reynolds number.

In order to solve the magnetostatic system of equations, ϕ is needed to be imposed (as a Dirichlet boundary condition) on the walls of the cavity. It is known that the magnetic field around a current carrying wire is only in the circumferential direction (see Fig. 8) where

$$B_\theta = \frac{\mu I}{2\pi d}. \tag{41}$$

Since $\mathbf{B} = -\mu\nabla\phi$, one can obtain ϕ as

$$\phi = -\frac{I\theta}{2\pi}. \tag{42}$$

Equation (42) provides the required boundary condition. Here, the length and the height of the cavity are $L = 20(m)$ and $H = 20(m)$, respectively, $\frac{I}{2\pi} = 14.5(A)$ and $D = 19(m)$. The magnetic solid body ($a = 2(m)$) is initially positioned at the center of the cavity. A relatively large value of the artificial speed of sound, $c_0 = 50000(m/s)$, is used to minimize oscillations due to the compressibility of the fluid at a vanishing Reynolds number. Figure 9 presents the time-history of the velocity of the solid body obtained for different domain resolutions. Magnetic flux density in the x-direction and pressure distribution along the centreline of the cavity ($y = 10(m)$) are shown in Figs. 10a and 10b for different a/δ_p at $t = 0.04(s)$. $\mathbf{B}$ deviates from Eq. (41) in the vicinity of the fluid-solid interface. Since results are obtained for a creeping flow, pressure has positive and negative values with the same absolute value in the front and the back of the moving body, respectively. In Fig. 10b, pressure results were shifted to possess a zero mean-value. Figures 11a and 11b present the corresponding profiles of the x-component of velocity along the vertical line $x = 10(m)$ and the centreline, respectively. A zero net mass-flux is obtained by integrating v_x along $x = 10(m)$ in Fig. 11a which confirms the mass conservation in a closed channel. It must be
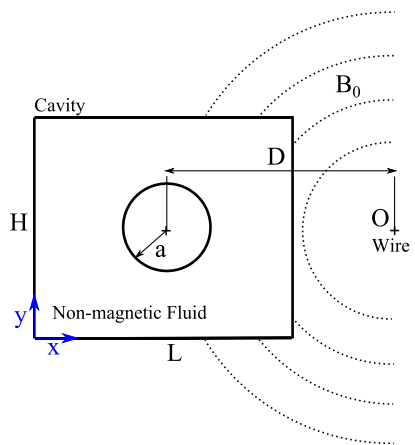
15

Figure 8: Schematic of the suspended solid body in a cavity. Contours of B_θ outside the cavity are shown by dotted lines.
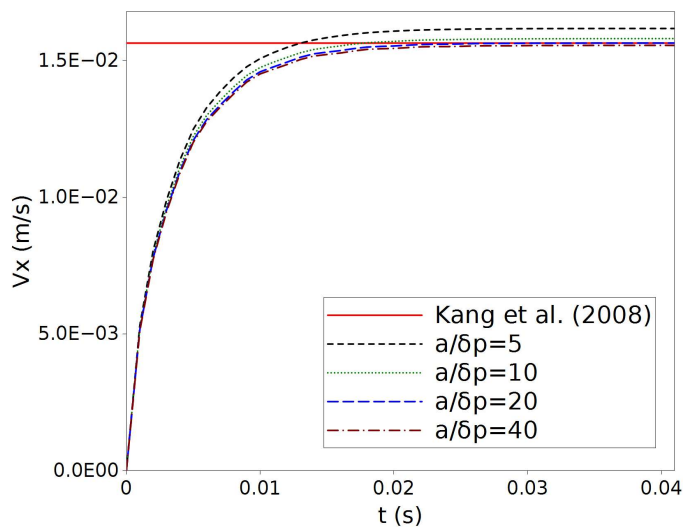

Figure 9: Time-history of the horizontal velocity of the suspended solid body in a cavity. FEM solution [21] in the Stokes regime is shown by a horizontal line.
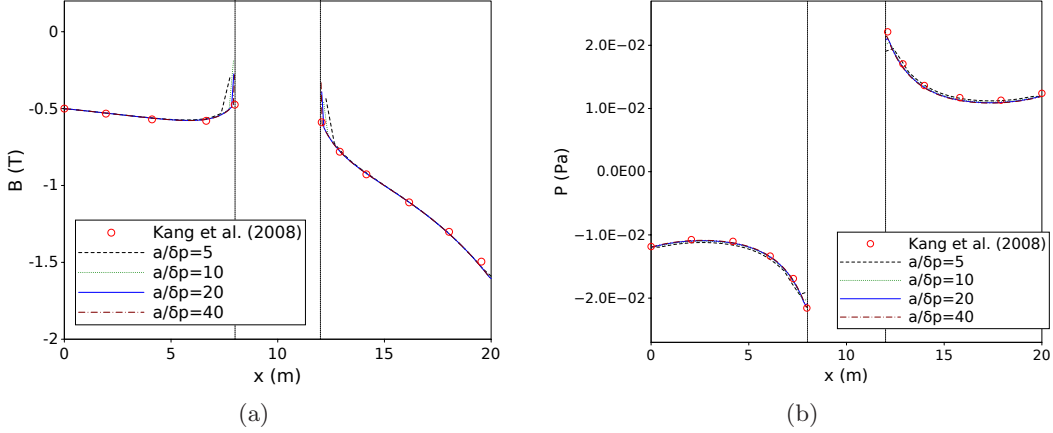
16

Figure 10: Profiles of (a) magnetic flux density and (b) pressure along $y = 10(m)$ in the cavity in comparison with [21] at $t = 0.04(s)$.

noted that, all these field variables are probed outside the circular cylinder. All results converged to the finite element solution reported in [21]. However, slight discrepancies adjacent to the solid boundary, at $x = 8(m)$ and $x = 12(m)$, are due to insufficient SPH resolution; $a/\delta_p = 5$ and 10.

4.2.1.1   Momentum Conservation

Although the present SPH method provides more accurate calculations of the spatial derivatives compared to the conventional SPH method, it does not guarantee the exact momentum conservation as is the case for conventional SPH [41, 42, 43]. This is due to a generally non-symmetrical formulation resulted from the renormalized spatial derivative schemes. Here, the global momentum conservation properties of the present hydrodynamic solver are investigated for a test-case with geometrical parameters similar to Fig. 8. As shown in Fig. 12, the external magnetic force is absent and the solid body starts moving due to a constant external force, **F** and a constant external moment **M**. All physical parameters are the same as the previous test-case except for the fluid viscosity, $\eta = 0.001(Pa.s)$, and the speed of sound, $c_0 = 200(m/s)$.

Numerical investigation of the global momentum conservation is performed by comparing the net force acting on the fluid domain, Ω_f, due to the presence of the solid boundaries, Γ_C and Γ_0, with the rate of momentum. The *Net Force* and the *Net Moment* are calculated as

$$Net\ Force = \int_{\Gamma_0} (p\mathbf{n} - \boldsymbol{\tau} \cdot \mathbf{n})\,dS + \int_{\Gamma_C} (p\mathbf{n} - \boldsymbol{\tau} \cdot \mathbf{n})\,dS, \qquad (43)$$

and

$$Net\ Moment = \int_{\Gamma_0} \mathbf{r} \times (p\mathbf{n} - \boldsymbol{\tau} \cdot \mathbf{n})\,dS + \int_{\Gamma_C} \mathbf{r} \times (p\mathbf{n} - \boldsymbol{\tau} \cdot \mathbf{n})\,dS. \qquad (44)$$

The integrals in Eqs. (43) and (44) are approximated by summations over boundary SPH particles in the same way as presented in Eqs. (30) and (31). The *Rate of Linear Momentum* and the *Rate of Angular Momentum* can be simply calculated as

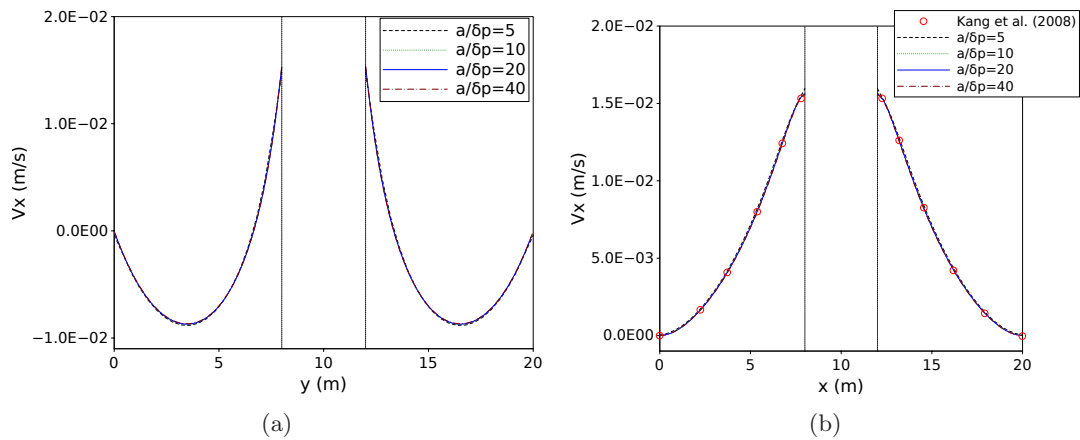$$Rate\ of\ Linear\ Momentum = \frac{d\sum_i m_i \mathbf{v}_i}{dt}, \qquad (45)$$

17

Figure 11: Velocity profiles in the cavity along (a) $x = 10(m)$ and (b) $y = 10(m)$ in comparison with [21] at $t = 0.04(s)$.
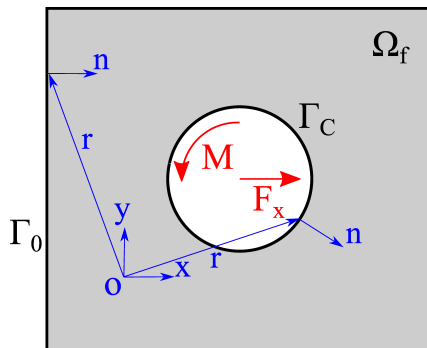

Figure 12: Schematic of a solid body confined in a rectangular cavity. The coordinate system is corresponding to origin o fixed in space.
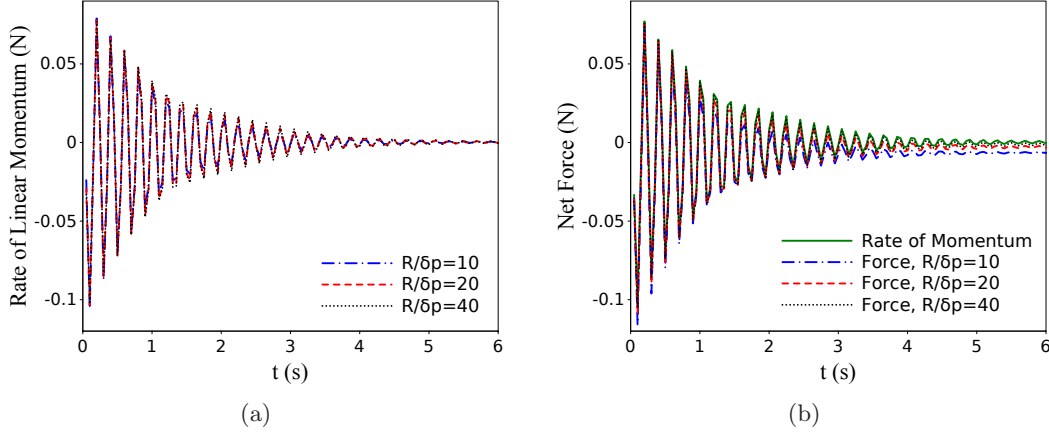
Figure 13: Time history of a) the *Rate of Linear Momentum*, and b) the *Net Force* in comparison with the *Rate of Linear Momentum* for different domain resolutions. Results are obtained for $|\mathbf{F}| = 0.1(N)$ in the x-direction with $\mathbf{M} = 0$.

and

$$Rate\ of\ Angular\ Momentum = \frac{d \sum_i m_i \mathbf{r} \times \mathbf{v_i}}{dt}, \qquad (46)$$

where i points to all fluid SPH particles positioned inside fluid computational domain Ω_f and $\frac{d}{dt}$ is discretized using a first order differencing scheme.

Figure 13a presents the time-history of the *Rate of Linear Momentum* for a case with $|\mathbf{F}| = 0.1(N)$ applied in the x-direction with $\mathbf{M} = 0$. As seen in this figure, there is no significant difference between the results obtained for different domain resolutions. Large oscillations at the beginning of the motion are resulted from the start-up pressure waves propagated in a rather small closed cavity due to the compressibility of the suspending fluid with a relatively small c_0. The rate of the total momentum gradually tends to zero as the solid body obtains a terminal velocity at $t \approx 5(s)$. The *Net Force* however, strongly depends on the resolution as observed in Fig. 13b. The difference between the calculated forces and the rate of momentum can be explained by the following points;

- The finer the resolution, the more accurate the calculation of the force acting on a solid boundary.

- Due to the shifting mechanism used in the present work, the *Net Force* calculated by integrating pressure and stress forces (see Eqs. (43) and (44)) is not exactly the same as the actual numerical force exerted on the fluid SPH particles.

- The first-order discretization of $\frac{d}{dt}$ is responsible for a transient error in the rate of momentum and can be reduced by decreasing the time-step. This automatically takes place by increasing the domain resolution according to Eq. (40).

Nevertheless, there is a good agreement between the *Rate of Linear Momentum* and the *Net Force* obtained for the finest domain resolution, $R/\delta_p = 40$. It must be noted that in this test-case with $|\mathbf{M}| = 0$, the *Rate of Angular Momentum* is practically zero (changes in the order of numerical error).
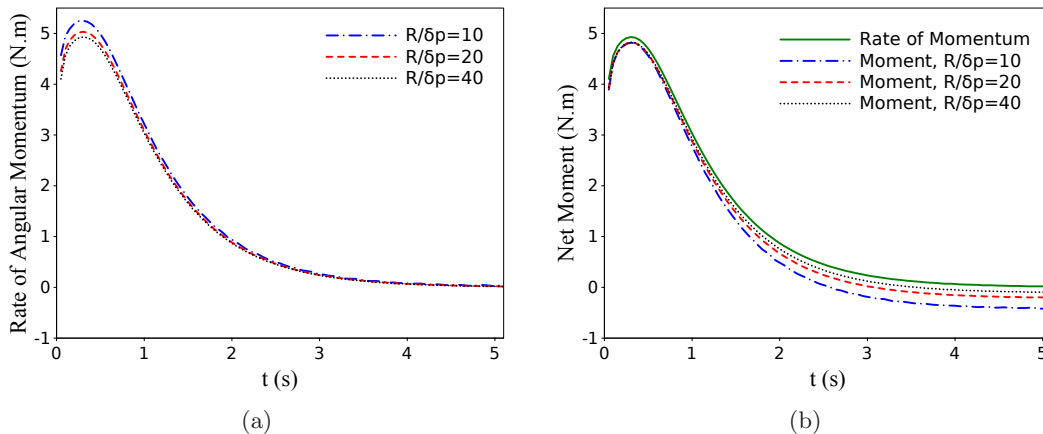
19

Figure 14: Time history of a) the *Rate of Angular Momentum*, and b) the *Net Moment* in comparison with the *Rate of Angular Momentum* for different domain resolutions. Results are obtained for $|\mathbf{F}| = 0.1(N)$ in the x-direction with $\mathbf{M} = 0$.

Similar study is performed for the global conservation of the angular momentum with $|\mathbf{M}| = 0.5(N.m)$ and $|\mathbf{F}| = 0$. The results are shown in Fig. 14. As seen in Fig. 14a, domain resolution affects the *Rate of Angular Momentum* mainly in the transient zone and the results converge to a single curve as the solid body almost obtains its terminal angular velocity at $t \approx 4(s)$. The *Net Moment* is however affected more by domain resolution at $t \geq 2(s)$ as observed in Fig. 14b. The difference between the *Rate of Angular Momentum* and the *Net Moment* can be explained with the same arguments as stated before. Therefore, it can be concluded that although the present method does not guarantee the exact momentum conservation, the global conservation properties are improved by increasing the resolution of the discretized domain. Since energy conservation itself is mainly affected by momentum conservation, similar behaviour is also expected for energy.

4.2.2. A Pair of Solid Bodies in a Closed Cavity

In the previous test-case, the present method was validated for a single solid body. Here, two neutrally buoyant paramagentic solid bodies suspended in a circular cavity are free to interact under the influence of an external magnetic field. This problem was first solved in [21] and became a benchmark for different numerical methods [19, 22]. The geometry of the present test-case is schematically similar to what was presented in Fig. 2.

Two circular cylinders of radius $a = 1(m)$ are positioned in the cavity $(R = 15a)$ with an initial angle of $\theta_0 = 60°$ and an initial distance of $2r_0 = 4a$. The external magnetic field is set to $|\mathbf{B_0}| = 1(T)$ and the problem is solved for $R/\delta_p = 15$. The density of the suspending fluid is $\rho = 1(kg/m^3)$ while different viscosities lead to different Reynolds numbers. In this test-case, the artificial speed of sound is set to $c_0 = 1(m/s)$. It should be noted that unlike all previous studies, here, the inertial effects are present. The Reynolds number is defined as $Re = \frac{\rho U_m a}{\nu}$, where U_m is a local maximum in the time-history of the velocity of solid bodies. Figure 15 shows the trajectory of P_1 for different Reynolds numbers in comparison with the result reported in [22] for a vanishing Reynolds number (Stokes flow regime).

Neglecting the fluid inertia, the trajectory of the solid bodies is a function of the initial configuration and only weakly depends on the physical properties [22]. Also, except for the case with
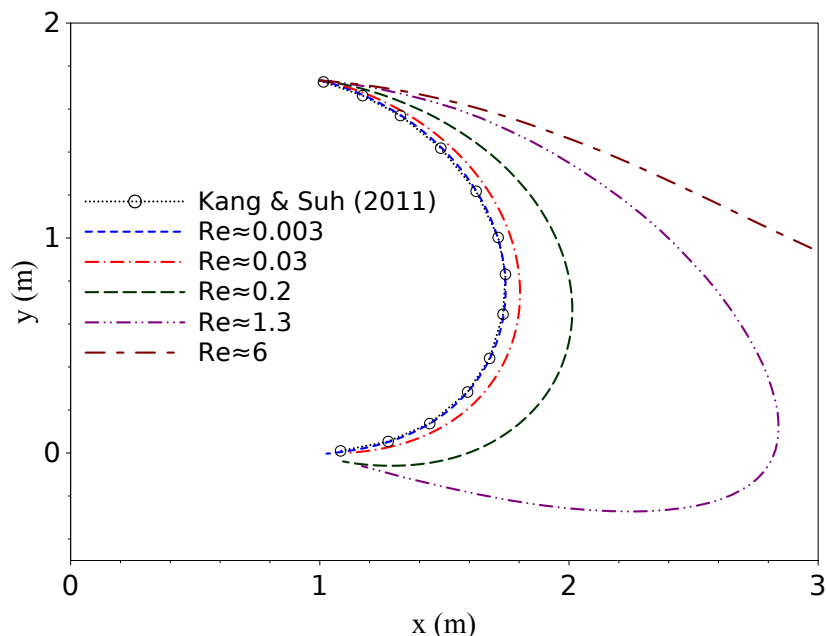
20

Figure 15: Two magneto-hydrodynamically interacting circular cylinders. Trajectories of the first solid body obtained for different Reynolds numbers in comparison with the result reported in [22].

$\theta_0 = 90°$, solid bodies are eventually paired and aligned with the external magnetic field [21]. However, as seen in Fig. 15, by increasing the inertia in the system, the trajectory expands and solid bodies travel a larger distance. In these cases, the solid bodies collide before aligning with the external magnetic field. In an extreme case when the Reynolds number is relatively large ($Re \approx 6$ in the present test-case), in the beginning of the motion while a repulsive magnetic force is active, two solid bodies are thrown to a rather large distance. In such a case, the magnetic attraction is too weak to overcome the inertia. Therefore, two solid bodies are eventually separated. At a fairly small Reynold number ($Re \approx 0.003$ in the present test-case), the trajectory is almost the same as that reported in [22] for the Stokes flow regime.

4.2.3. Magnetic Chain in a Rotating Magnetic Field

In the previous test-cases, the present method was verified for a single solid body and a pair of interacting paramagnetic circular cylinders. Here, the performance of the present SPH method is investigated in a test-case which involves the rupture (and possibly the reformation) of a magnetic chain. Nine ($N = 9$) neutrally buoyant paramagnetic solid bodies are suspended in a circular cavity of radius $R = 0.0175(m)$ filled with a non-magnetic fluid and the system is subjected to a rotating ($\omega = \pi(Rad/s)$) external magnetic field. The circular cylinders ($a = 0.00125(m)$) are initially positioned in a row aligned with the external magnetic field with $Gap = \delta_p$, as schematically shown in Fig. 16. Here, the fluid domain is marked with two different colours for a more clear illustration of the motion of the fluid SPH particles.

A direct numerical simulation of a similar problem was first reported in [1], however, at a vanishing Reynolds number. When the external magnetic field starts rotating, depending on the
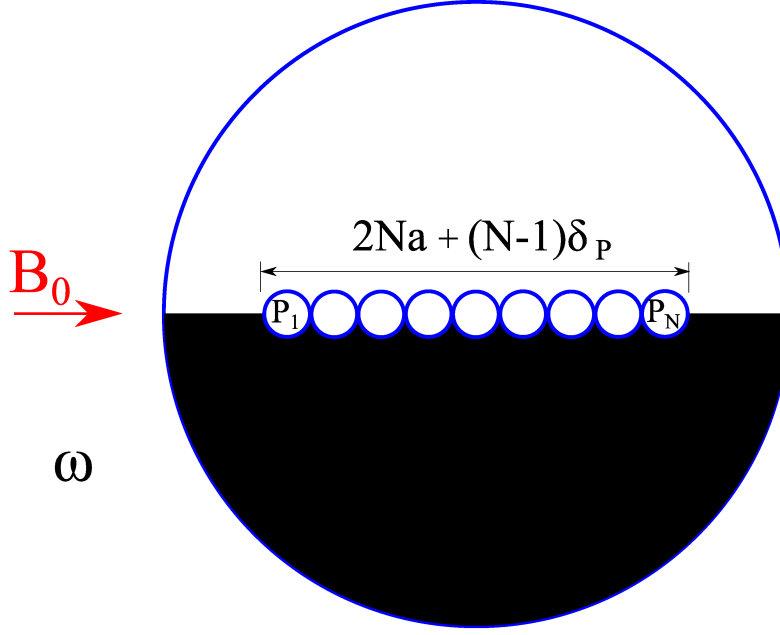
21

Figure 16: Initial configuration of the magnetic solid bodies forming a chain confined in a circular cavity.

ratio of the hydrodynamic forces (due to viscosity) to the magnetic forces [16], either an almost rigid rotation (low ratio) or a fixed magnetic chain (high ratio) is observed [1]. In other cases, however, the magnetic chain broke into multi-chains of shorter lengths [44]. In this problem, the Mason number as a measure of the ratio of the viscous forces to the strength of the magnetic field is defined as [21]

$$Mn = \frac{\eta\omega}{(\mu_s - \mu_f)H_0^2}, \tag{47}$$

where $H_0 = |\mathbf{B}_0|/\mu_f$.

In this work, inertial effects are also present and this test-case is solved for three different Reynolds numbers. In all cases, $a/\delta_p = 18.75$ and $F_0 = 0.01(N)$ which is high enough to prevent a numerical failure due to a solid-solid collision. The artificial speed of sound is $c_0 = 2(m/s)$, except for the case with $Re = \frac{\rho(R\omega)a}{\eta} = 0.172$ which is solved with $c_0 = 5(m/s)$. The magnetic susceptibility is $\chi = 0.1$ with $\mathbf{B}_0 = 6(T)$. Figure 17 presents the snapshots of the configuration of the initially straight magnetic chain. The Mason number is kept constant for this set of results, $Mn = 0.00087$, while the Reynolds number is changed by altering the density. As seen in this figure, the configuration highly depends on the inertia of the system even for a rather small Reynolds number, $Re < 1$. The magnetic chain has a S-shaped configuration [45] at the very first instances of motion. The chain rupture happens in all cases, however, the chain reformation is only observed for the smallest Reynolds number, $Re = 0.172$, as shown in Fig. 17g. As discussed above for two interacting bodies, the higher the Reynolds number, the more likely the separation of the magnetic solid bodies during a magneto-hydrodynamic interaction. This explains why there is a less chance for chain reformation at larger Reynolds numbers.
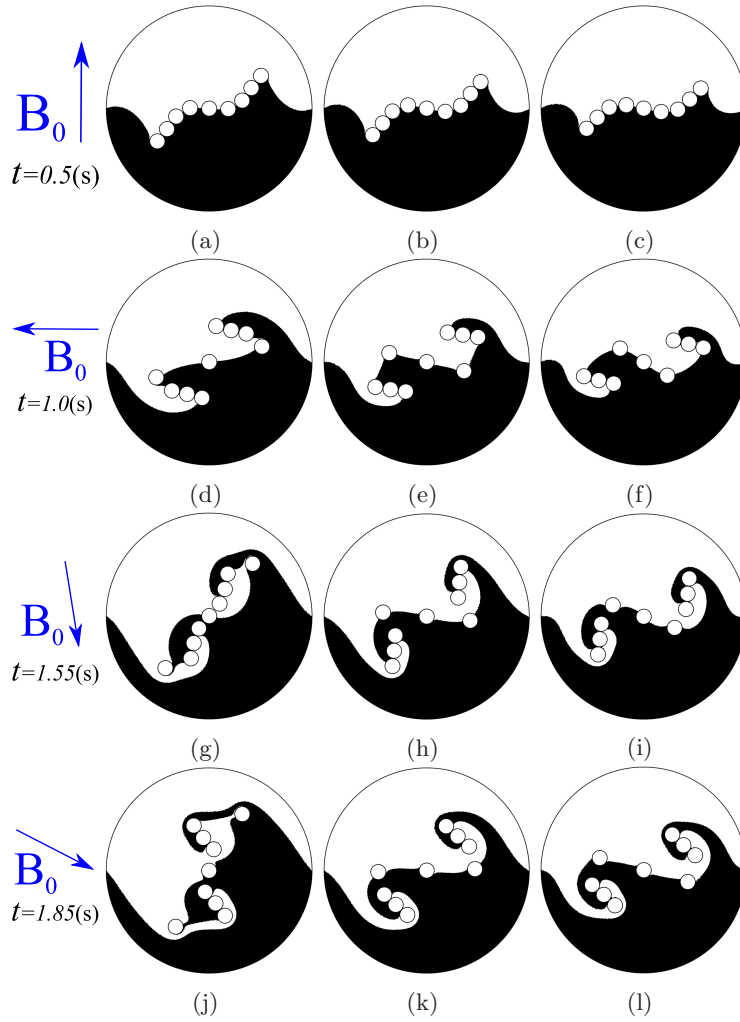
22

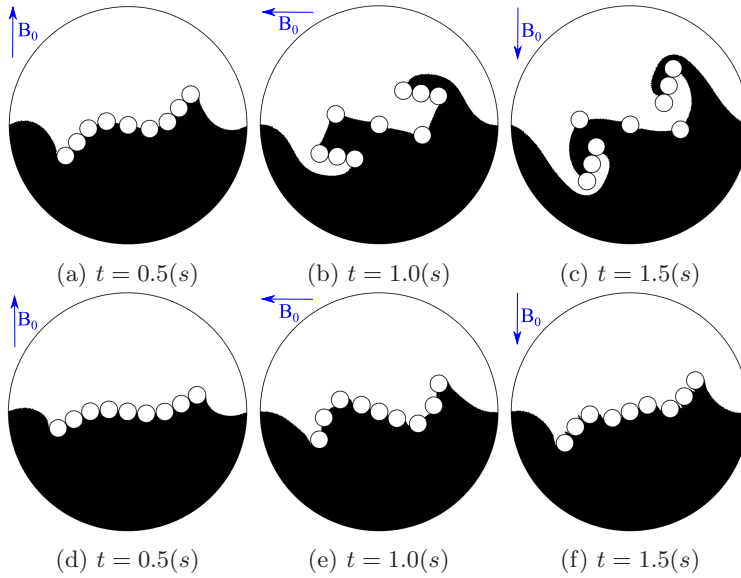Figure 17: Snapshots of the configuration of the solid bodies in a circular cavity under the influence of a rotating magnetic field. The direction of the external magnetic field for each row of sub-figures are shown on the left. (a),(d),(g), and (j) present the results obtained for $Re = 0.172$, (b),(e),(h), and (k) correspond to $Re = 0.344$, and the results obtained for $Re = 0.687$ are shown by (c),(f),(i), and (l).

23

Figure 18: Snapshots of the configuration of the solid bodies in a circular cavity under the influence of a rotating magnetic field. Results are presented for $Re = 0.344$. (a),(b), and (c) present the results obtained for $Mn = 0.00087$, and (d),(e), and (f) correspond to $Mn = 0.00174$. The direction of the external magnetic field is shown at the top-left corner of each sub-figure.

Table 2: Computational costs and allocated memories for different domain resolutions.

a/δ_p	Number of particles	$CPU - time/step(s)$	Memory (MB)
6.25	21935	0.11	60
12.5	87016	0.39	220
18.75	195181	0.91	500
25	346663	1.6	900

Figure 18 illustrates the results obtained at the same Reynolds number, $Re = 0.344$, for two different Mason numbers, $Mn = 0.00087$, and $Mn = 0.00174$. It must be noted that the Mason number is changed by altering the fluid viscosity. By increasing the Mason number, solid bodies are more affected by hydrodynamic forces. This leads to a larger time-lag between the alignment of the chained solid bodies and the rotating magnetic field. In Fig. 18, for $Mn = 0.00174$, a rather large time-lag prevents the complete rotation of the structures formed by the magnetic solid bodies. In this way, no mixing mechanism is observed.

The CPU-time and the allocated memory are shown in Table 2 for different domain resolutions. The computations were conducted on a 3rd generation Intel® Core™ i7 CPU at 3.8 GHz. It must also be noted that the allocated memory slightly changes during a simulation due to the construction and the deconstruction of the auxiliary variables used in the programming of the present method.

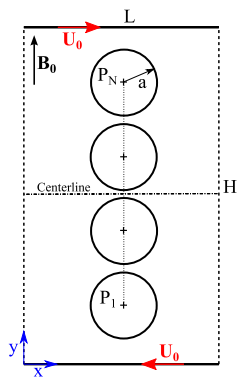*4.3. Application: Magnetic Chain in a Periodic Shear Flow*

Figure 19: Schematic of a magnetic chain formed by N circular solid bodies in a periodic shear flow.

In the following, the proposed SPH method is used to simulate the effect of shear on a chain formed by magnetic solid bodies under the influence of a constant magnetic field. The main goal is to investigate the applicability of the proposed method in a more complex test-case resembling a real-world situation in magnetorheological fluids. A similar problem was first solved by Kang *et al.* [23] using the finite element method in the Stokes flow regime.

In the initial configuration, solid bodies P_i $(i = 1, \cdots, N)$ are evenly arranged vertically in a periodic channel with a gap $(= \delta_p)$ in between as schematically illustrated in Fig. 19. The upper and lower walls are moving with velocities of the same magnitude (U_0) in opposite directions. This gives a shear rate of $\dot{\gamma} = 2U_0/H$. The circular solid bodies are of the same size $(a = 0.00125(m))$ and the height of the channel is $H = 20a$. In all test-cases, the magnetic susceptibility of the suspended solid bodies and dynamic viscosity are kept constant; $\chi = 0.1$ and $\eta = 0.01(Pa.s)$, respectively. Unless otherwise mentioned, solid bodies are neutrally buoyant, $N = 9$, $a/\delta_p = 18.75$ and the coefficient of repulsive force is $F_0 = 0.1(N)$. It must be noted that, this value of F_0 is high enough not to let solid bodies come into contact with a Gap smaller than $0.5h_c$.

Figures 20a and 20b show the time history of the velocity of P_1 obtained for $Re = \frac{2\rho U_0 H}{\eta} = 5.0$, $L = 0.01(m)$ and $B_0 = 10(T)$, respectively in x-direction and y-direction for three different domain resolutions. It is observed that for $a/\delta_p \geq 18.75$, results have converged. Disturbances seen in the vertical velocity occur at the very beginning of the simulation due to the solid-solid collisions. These collisions are sensitive to the domain resolution which defines the initial gap between solid bodies and the cut-off distance h_c used in the definition of the repulsive force.

It should be emphasized that, although in some applications, *e.g.* microfluidic devices, the particle Reynolds number defined at the scale of a suspended solid body is $Re_p = \frac{\rho \dot{\gamma} a^2}{\eta} << 1$, inertia becomes important in dynamic loadings at a high frequency [46]. Figure 21 displays the effect of inertia on the evolution of the velocity of P_1 in x-direction. In order to change Re, density is changed while all other parameters corresponding to either the magnetic force and the viscous effect [16] are kept constant.

At a low Reynolds number, shear effects soon diffuse from the moving wall into the domain due to a dominant viscosity. Magnetic chain is tilted from its initially vertical configuration with solid bodies moving at almost the same pace as the local fluid until a steady-state is reached. At steady-state, the magnetic torque externally induced on the chain balances the viscous torque due
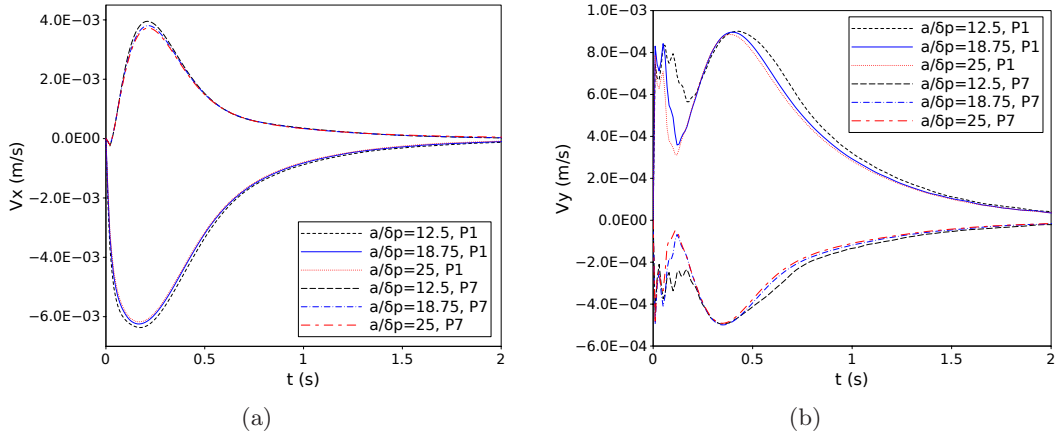
25

(a)   (b)

Figure 20: Convergence of velocity of $P1$ and $P7$ in the (a) x-dirction and (b) y-direction for $Re = 5$ and $B_0 = 10(T)$.
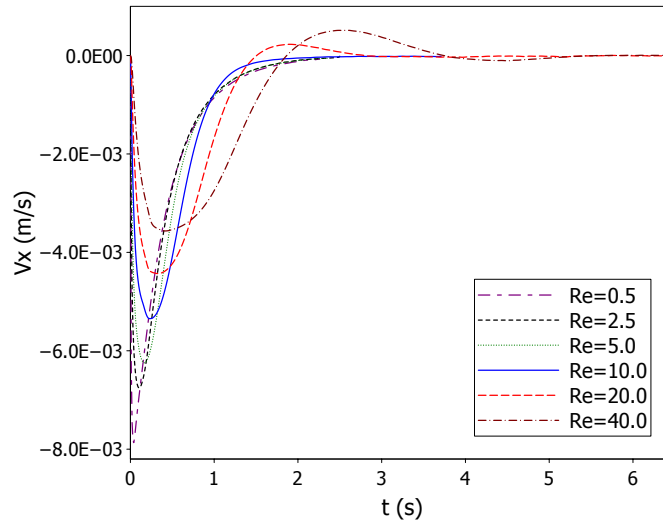

Figure 21: The effect of inertia on the time-history of the velocity of solid body P_1 in the x-direction.
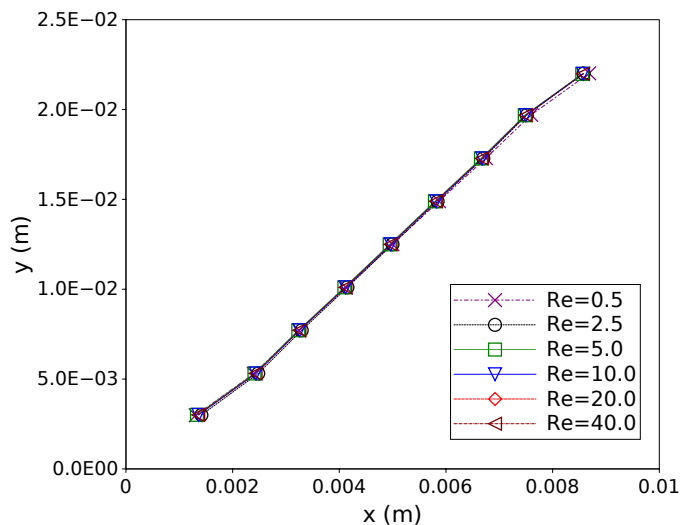
26

Figure 22: Steady-state shape of the magnetic chain obtained at different Reynolds numbers.

to shear [16]. By increasing Re, it takes longer time for shear effects to be diffused in the domain. Also, inertia affects the balance of magnetic and hydrodynamic forces acting on a solid body as its momentum changes. Inertial effects are only present in the time-history of the motion and the steady-state results are not significantly affected by increasing Re. The steady-state configuration of the solid bodies in a magnetic chain is shown in Fig. 22. As expected, the arrangements of the solid bodies are almost identical for different Reynolds numbers.

Streamlines are plotted for $Re = 2.5$ and 40 in Figs. 23 and 24, respectively. At $Re = 2.5$ the magnetic chain is gradually tilted following the fluid flow. However, as seen in Fig. 24a for $Re = 40$, the shear deformation of the chain is started from tips. Flow patterns at the steady-state are almost the same for both Reynolds numbers, but stronger vortices are observed in Fig. 24c. It must be noted that the corresponding particle Reynolds numbers are $Re_p = 0.00625$ and 0.1, respectively for $Re = 2.5$ and 40. In all of the following simulations unless otherwise mentioned, Reynolds number is $Re = 5.0$ which gives a particle Reynolds number of $Re_p = 0.0125$.

4.3.1. Effect of Solid Volume Fraction

In this section, the external magnetic field density is $B_0 = 10(T)$ and the periodic length of the channel, L, is a variable controlling the solid volume fraction as

$$\Phi = \frac{N\pi a^2}{LH}. \tag{48}$$

By increasing Φ, although the adjacent magnetic solid bodies from a chain its periodic image do not come into contact for parameters chosen in this work, the flow pattern is significantly affected and the chain is less prone to tilting. However, by decreasing Φ, since the system is gradually approaching a single chain in a shear flow, an asymptotic configuration is expected. Figure 25 shows the steady-state magnetic chain configuration for different solid volume fractions.

In the following, the effect of solid volume fraction on the apparent viscosity of the system is investigated. To this end, average of the shear stress exerted on the bottom wall of the channel,
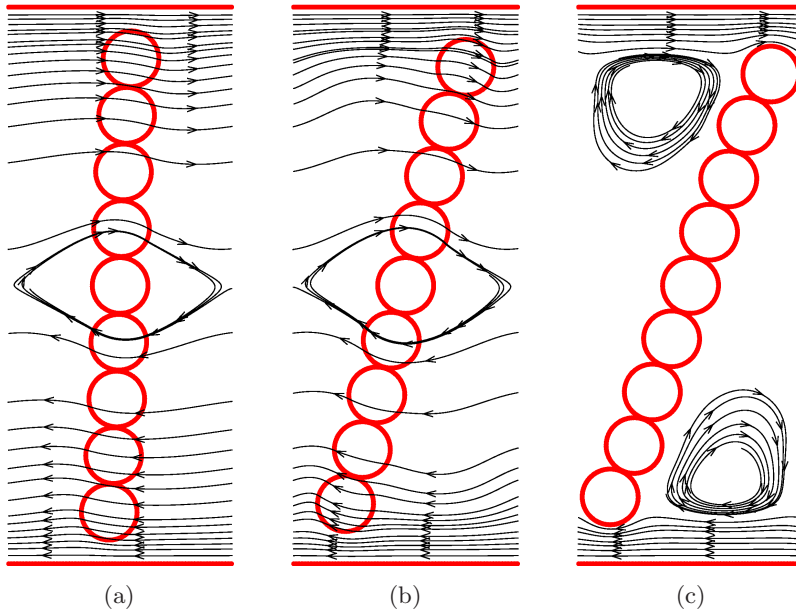
27

Figure 23: Streamlines around a magnetic chain obtained for $Re = 2.5$, plotted at (a) $t = 0.2(s)$, (b) $t = 0.6(s)$, and (c) steady-state.
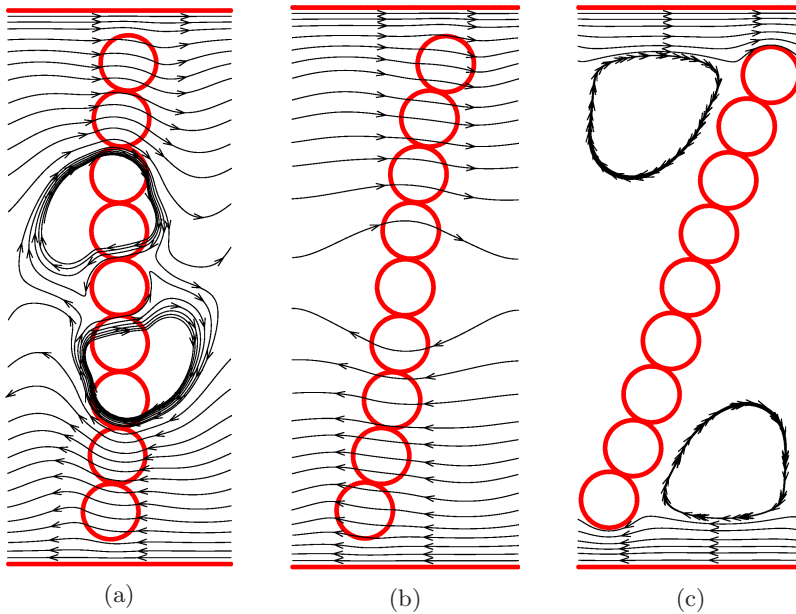

Figure 24: Streamlines around a magnetic chain obtained for $Re = 40.0$, plotted at (a) $t = 0.2(s)$, (b) $t = 0.6(s)$, and (c) steady-state.
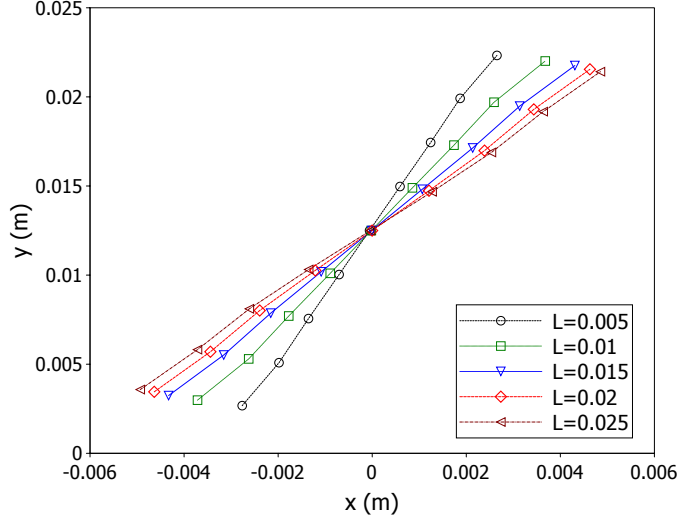
28

Figure 25: The effect of periodicity length on the steady-state shape of the magnetic chain.

$y = 0.0(m)$, is divided by the strain rate as

$$\eta_a = \frac{\bar{\tau}_{xy}}{\dot{\gamma}} = \frac{1}{\dot{\gamma}L} \int_{y=0} \tau_{xy} dx. \tag{49}$$

Therefore, according to Eq. (49) the shear force acting on the wall of the channel is equal to $\eta_a \dot{\gamma} L$. Results are shown in Fig. 26 as a function of L. As one expected, the apparent viscosity is directly related to the inverse of the tilting angle. The more the tilting angle, the more the space for the fluid to flow in the channel. Therefore, by increasing the length of periodicity, the apparent viscosity is reduced. As discussed above for the tilting angle, an asymptotic value of η_a is also expected by letting $L \to \infty$.

4.3.2. Effect of Mason Number

The formation of microstructures in a magnetorheological fluid is determined by a competition between hydrodynamic interactions and magnetic forces [47]. Therefore, Mason number is introduced to quantify these effects as the ratio of a characteristic viscous force to the magnetic (polarization) force [23]

$$Mn = \frac{\eta \dot{\gamma}}{\mu_0 \beta^2 H_0^2}, \tag{50}$$

where $\beta = \frac{\chi}{3+\chi}$ is the effective polarization for a spherical magnetic body. Steady-state configuration of the magnetic chain for $Re_p = 0.0125$ and $L = 0.01$ is shown in Fig. 27 for different Mason numbers. Here, only the external magnetic field is changed, while all other parameters are kept constant. The corresponding apparent viscosities are presented in Fig. 28.

By decreasing Mn, tilting angle is reduced until the magnetic chain holds an almost vertical orientation. Regarding the configuration of the magnetic chain, the apparent viscosity is therefore increased up to a maximum which corresponds to an almost vertically oriented chain observed in
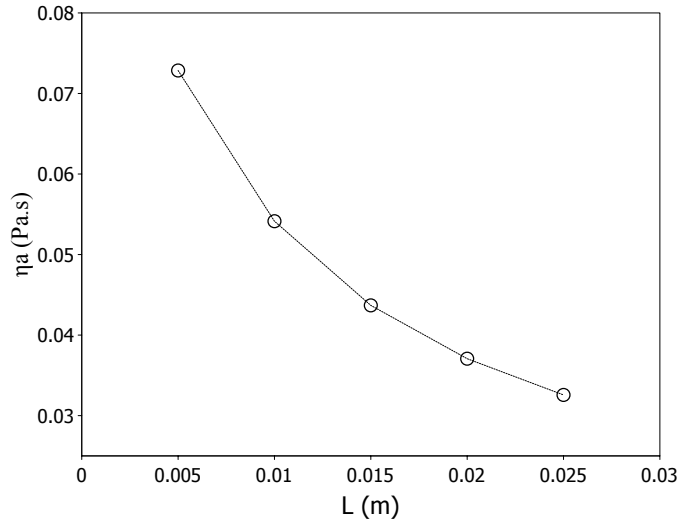
29

Figure 26: Apparent viscosity as a function of periodicity length.
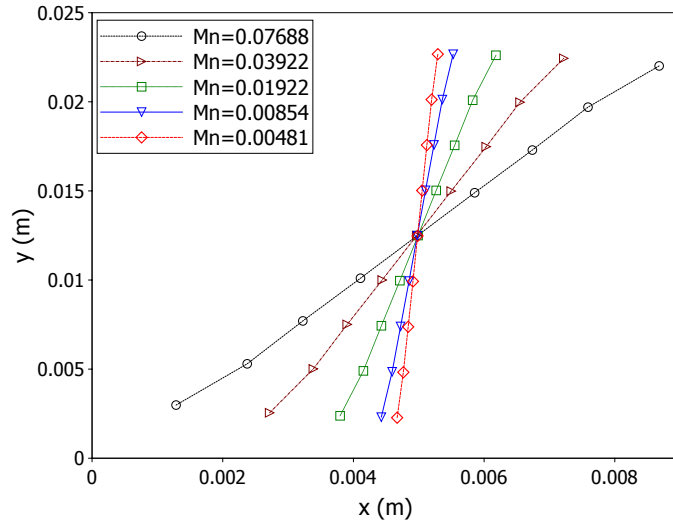

Figure 27: The effect of Mason number on the steady-state shape of the magnetic chain.
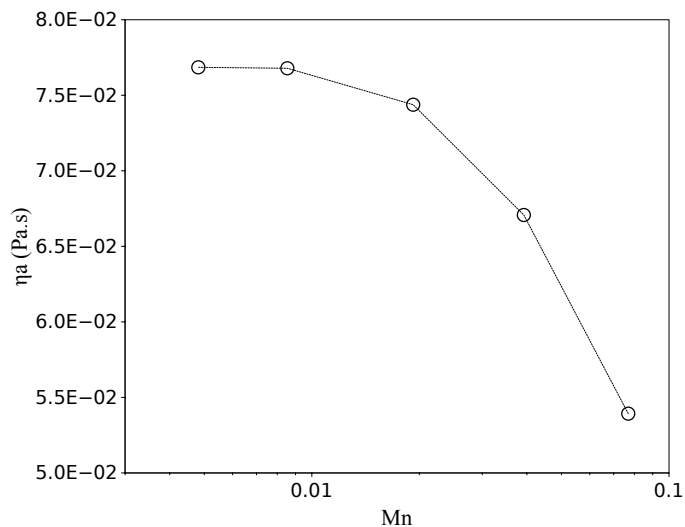
30

Figure 28: Apparent viscosity as a function of Mason number.

Figs. 27 and 28 for $Mn \leq 0.0085$. These results are in a qualitative agreement with those reported in [23].

It must be noted that for very low Mason numbers, although a stiff repulsive force (32), *i.e.* $F_0 >>$ magnetic force, prevents solid bodies to come into a close contact, it will lead to numerical instabilities in a long-time simulation. However, this difficulty can be treated by either using a soft repulsive force or implementing an implicit procedure as introduced in [37].

In general, it is more useful to define Mason number in a way that includes the presence of neighbouring suspended magnetic solid bodies [47]. In 2012, Gao *et al.* [16] introduced a modified dimensionless parameter which was the ratio of the viscous torque to the magnetic torque acting on a chain of solid bodies. In their work, the number of magnetic solid bodies incorporating in the formation of a magnetic chain, was reported to be an important factor. Figure 29 shows the steady-state shape of a magnetic chain under shear for different number of solid bodies forming the chain. As observed in Fig. 29, by decreasing N the tilting angle is decreased. This is due to a direct relation between the hydrodynamic torque and the length of a chain deforming in a shear flow. Nevertheless, the tilting angle is almost the same for $N = 5$, 3 and 2. Note that, the larger blockage ratio for a longer chain is also an important factor in increasing the tilting angle.

4.3.3. Small Amplitude Oscillatory Shear

In this section, oscillatory velocities ($U = \pm U_0 \cos(\omega t)$) are imposed on the top and the bottom walls of the channel. In this way, shear strain is $\gamma = \gamma_0 \sin(\omega t)$, where $\gamma_0 = U_0/H\omega$. Dynamic viscoelastic response of magnetorheological fluids has been experimentally investigated under small [30] and large amplitude oscillatory shears [48]. Here, the effect of Mason number on the viscoelastic behaviour of a periodic array of magnetic chains suspended in a Newtonian fluid is investigated.

In the absence of inertia, the stress response of a complex system to Small Amplitude Oscillatory Shear (SAOS) can be considered sinusoidal with the same frequency, ω, as [49]

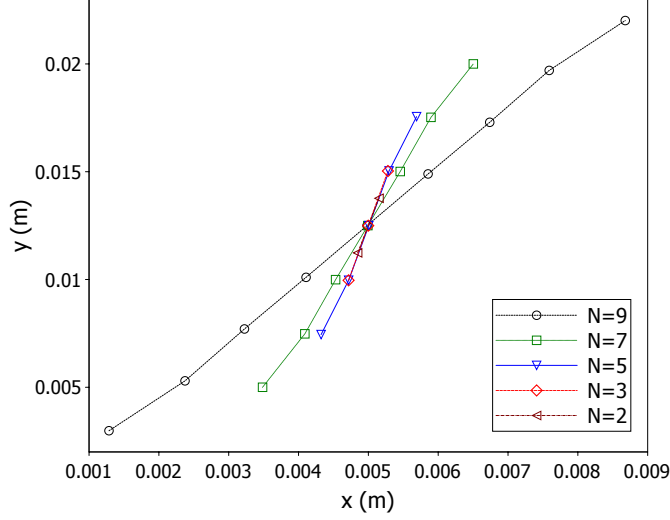$$\bar{\tau}_{xy} = \tau_0 \sin(\omega t + \psi). \tag{51}$$

31

Figure 29: Steady-state shape of the magnetic chain formed by different number of solid bodies.

In Eq. (51), phase angle $0 \leq \psi = tan^{-1}(G''/G') \leq 90°$ defines the linear viscoelastic behaviour of the system, where $G' = (\tau_0/\gamma_0)\cos\psi$ and $G'' = (\tau_0/\gamma_0)\sin\psi$ are the storage and the loss moduli of the system, respectively. In a complex notation ($\gamma = \gamma^*\exp(i\omega t)$), one obtains

$$\bar{\tau}_{xy} = G^*\gamma, \tag{52}$$

where $G^* = G' + iG''$ is the complex shear modulus [50]. A completely out of phase response; $\psi = 90°$, corresponds to a pure viscous fluid and $\psi = 0$ denotes an elastic solid-like behaviour.

A non-zero inertia in dynamic rheometry results in storage of the kinematic energy in moving phases. Thus at a finite Reynolds number, both the suspending fluid and the suspended solid bodies are moving out of phase with the strain rate [51]. This is observed as a phase angle between stress and the strain rate even for a pure Newtonian fluid under SAOS [52], *e.g.* $46.3°$ for parameters used in this section with $Re = \rho U_0 H/\eta = 5$ in the absence of solid bodies (see [53] for details). Therefore, phase angles $\psi > 90°$ observed in the present work reveal the effect of inertia as well as the viscoelasticity of the system. Nevertheless, since the inertia (Reynolds number) is kept constant, the viscoelasticity of the system can be qualitatively investigated by studying ψ as a function of Mason number. To this end, it is required to fit a sine function in the spatially averaged shear stress, $\bar{\tau}_{xy}$, as shown in Fig. 30 for $Mn = 0.0534$, $\omega = 2\pi(Rad/s)$ and $Re_p = 0.0125$ ($Re = 5$). It is observed in Fig. 30 that $\bar{\tau}_{xy}$ is sinusoidal with the same frequency as γ. Therefore, the amplitude of the oscillatory shear is small enough for this system to remain in the linear viscoelastic range. Figure 31 presents phase angle as a function of Mason number. By increasing the external magnetic field (smaller Mason numbers) the elasticity increases which is observed as an increasing phase angle with Mn in Fig. 31. There is a steeper change in the phase angle near $Mn = 0.04$. Similar observation was reported in [30].

In Fig. 32, τ_0 is shown as a function of Mason number. The maximum shear stress is supposed to be corresponding to the maximum allowable deformation of the magnetic chain under oscillatory shear which is presented in Figure 33 for P_1 positioned at the bottom of the chain. As seen in
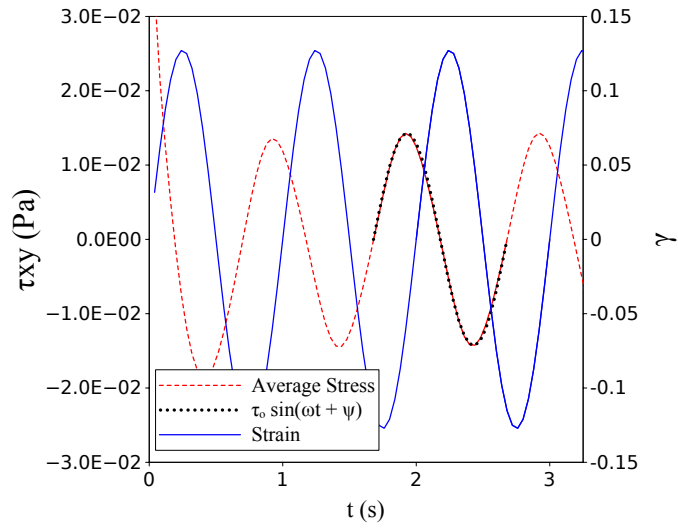
32

Figure 30: Average shear stress and strain in time for a magnetic chain under SAOS for $Re_p = 0.0125$, $Mn = 0.0534$, and $\omega = 2\pi (Rad/s)$.

Figure 31: Phase angle as a function of Mason number for $Re_p = 0.0125$ and $\omega = 2\pi (Rad/s)$.

33

Figure 32: Maximum shear stress as a function of Mason number for $Re_p = 0.0125$ and $\omega = 2\pi(Rad/s)$.

Figure 33: Maximum horizontal distance swept by P_1 as a function of Mason number for $Re_p = 0.0125$ and $\omega = 2\pi(Rad/s)$.

34

Figure 34: Average shear stress and strain in time for a magnetic chain under SAOS for $Re_p = 0.00625$, $Mn = 0.0534$, and $\omega = 2\pi(Rad/s)$.
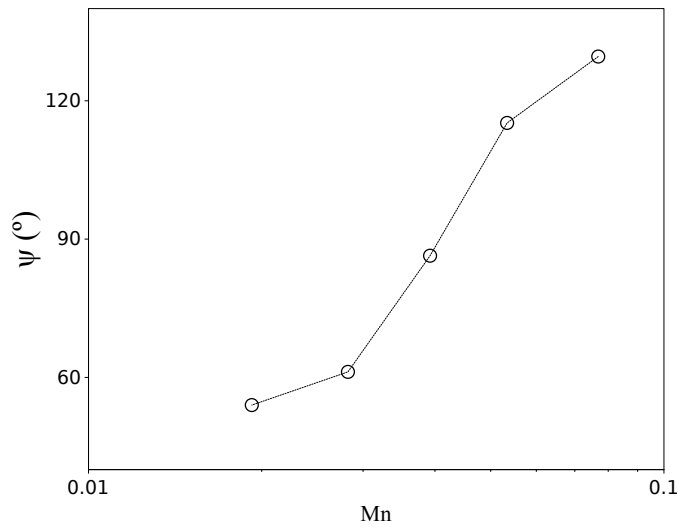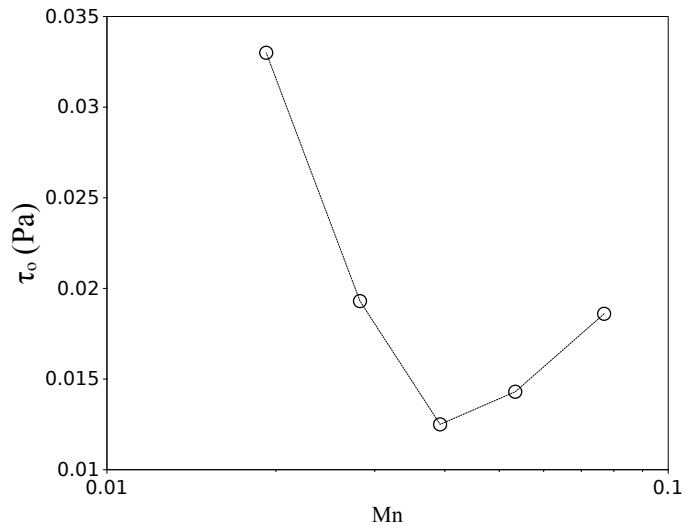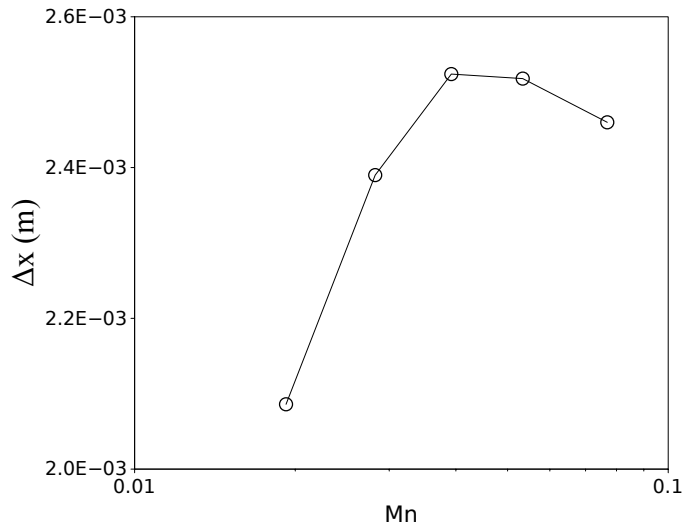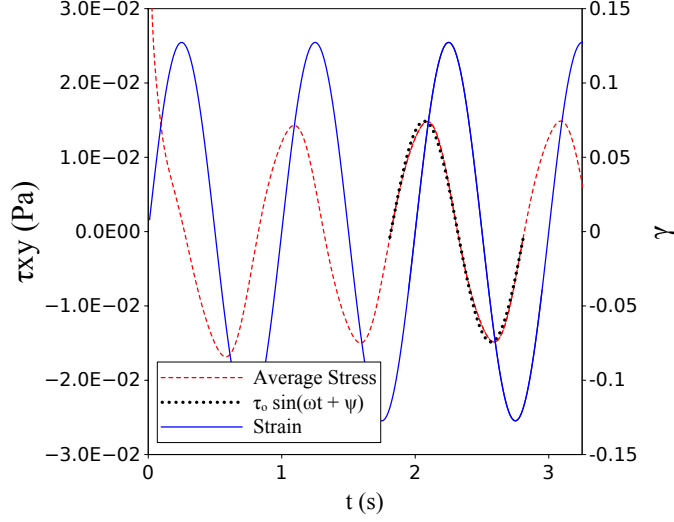
Figs. 32 and 33, the larger the tilting of the magnetic chain, $\Delta x/H$, the smaller the maximum shear stress, τ_0. Despite expectations, no monotonically ascending τ_0 is observed by increasing the external magnetic field. Such non-monotonic response may be explained by dominant inertial effects for higher Mn. In these cases, since $\psi > 90°$, the magnetic torque acting on the chain is added to the viscous effects preventing the suspended solid bodies from moving out of phase with the externally imposed shear. By further increasing the external magnetic field for $Mn < 0.04$, magnetic forces dominate the inertial effects. In this range of Mn, τ_0 increases as Mason decreases.

In order to specify the inertial effects on the results, similar investigations were made for $Re_p = 0.00625$. It must be noted that, all parameters are kept constant except density which is reduced by a factor of 0.5. A typical response is shown in Fig. 34 for $Mn = 0.0534$. In this case, the phase angle is reduced and τ_0 is slightly increased (from $0.0143(Pa)$ to $0.0149(Pa)$) in comparison with Fig. 30. As seen in Fig. 34, shear stress slightly deviates from the predicted sinusoidal response, $\tau_0\sin(\omega t + \psi)$, at its peaks. This may reflect the onset of a non-linear response. Figure 35 shows the Lissajous curves obtained for $Re_p = 0.00125$. It is observed that the shear stress-strain curves take almost elliptic shapes after some initial transitions. This confirms the presumption of the linear viscoelastic behaviour of system. Slope at zero shear strain, $G' = \frac{\partial \bar{\tau}_{xy}}{\partial \gamma}|_{\gamma=0}$ [54], slightly increases and the area enclosed by a curve, $E_d = \oint \bar{\tau}_{xy}d\gamma$, grows monotonically as the Mason number is reduced. Therefore, the elastic (storage) shear modulus of the system is increased and a more elastic behaviour is expected by increasing the external magnetic field. Also, the loss modulus, $G'' = E_d/\gamma_0^2\pi$ [54], increases by decreasing Mn. In this case, for $Re_p = 0.00625$, unlike the previous test-cases solved for $Re_p = 0.0125$, τ_0 grows monotonically with reducing Mn. As previously discussed, such a monotonic growth in τ_0, can be explained by an always less than 90° phase angle. These results are in agreement with conclusions made in [30].
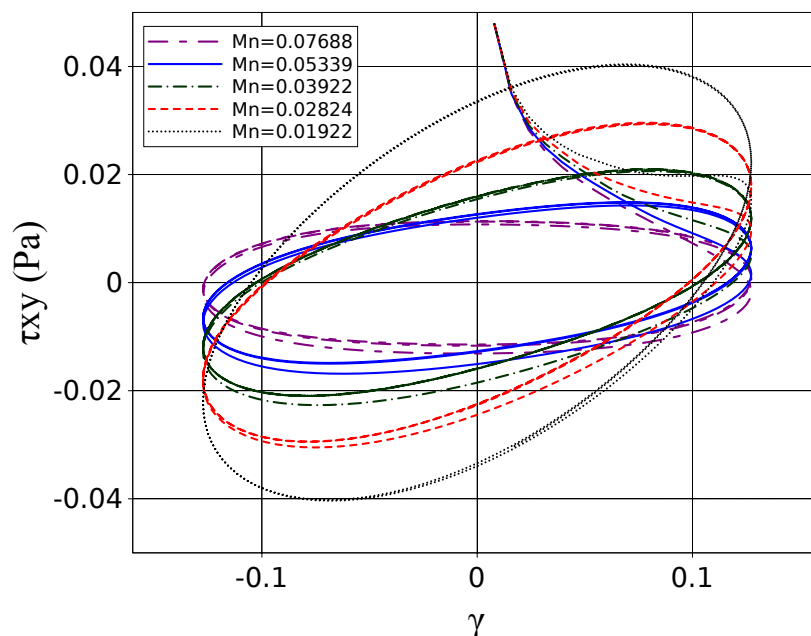
35

Figure 35: Lissajous curves obtained for $Re_p = 0.00625$ and $\omega = 2\pi(Rad/s)$.

5. Conclusion

A consistent WC-SPH method was developed to simulate the motion of para-magnetic solid bodies in a Newtonian fluid flow. The performance of the proposed method was first investigated by solving a magnetostatic problem and it was shown that the SPH method is a viable choice for such problems. Accurate values of the magnetic force acting on a solid body were obtained using a modified form of the Maxwell stress tensor. It was revealed that, the numerical error in the magnetic interaction of solid bodies is increased either by reducing the gap between approaching solid surfaces or increasing the magnetic susceptibility. For parameters chosen in this work (with $\chi \leq 1$), $Error$ was less than 4% with respect to the results of a FEM simulation with a boundary fitted mesh. The proposed algorithm was then tested against a benchmark problem in which both magnetic and hydrodynamic effects are present. A relatively large value for the artificial speed of sound was used in order to obtain satisfactory results at a vanishing Reynolds number. The error in the convergent solution was less than 0.5% with respect to the FEM solution reported in [21]. In another test-case, the proposed method was verified for two magneto-hydrodynamically interacting solid bodies suspended in a closed cavity. It was shown that inertia can lead to the separation of the magnetic solid bodies. The performance of the proposed method in simulating the evolution of a magnetic chain was also shown for a magnetic chain of circular cylinders under the influence of a rotating magnetic field. It was shown that the Reynolds number as well as the Mason number control the configuration of a magnetic chain.

A magnetic chain of solid bodies was simulated in a periodic shear flow. The effect of Reynolds number on the evolution of the chain was studied. It was shown that the inertia of the system only affects the time-history of the migration of solid bodies. Similar studies were conducted to

36

investigate the effects of the solid volume fraction and the Mason number. At low solid volume fractions, when the configuration of the magnetic solid bodies is more like a single chain deformed in a shear flow, an asymptotic behaviour in the apparent viscosity was observed. By decreasing the Mason number, tilting angle is reduced until the magnetic chain acquires an almost vertical orientation, for which the apparent viscosity reaches a plateau. Similar studies were conducted for magnetic chains of smaller lengths. The smaller the length, the lower the hydrodynamic torque. Thus, by reducing the number of solid bodies forming a magnetic chain (N), smaller tilting angles were obtained. However, in this work, the tilting angle was observed to be almost constant for $N \leq 5$.

In the last test-case, a periodic array of magnetic chains was investigated under SAOS. Results were obtained for two different Reynolds numbers $Re_p = 0.0125$ and 0.00625. The elastic response was observed to be decreasing with increasing the Mason number for both Reynolds numbers. For $Re_p = 0.00625$, the magnitude of the complex shear modulus was found to be monotonically increasing by increasing the external magnetic field. For higher Reynolds numbers, a non-monotonic behaviour was observed.

Acknowledgement

Appendix I - Magnetic Force Density

In this appendix, following [19], the magnetic force per unit length (area in three-dimensions) (33) is derived for a given scalar magnetic potential, ϕ. The net magnetic force acting on solid body s is calculated by integrating (16) over its area (volume in three dimensions), Ω_s, including its interface with the suspending fluid, $\partial \Omega_s$, as

$$\mathbf{F}_s^m = -\frac{1}{2} \int \int_{\Omega_s} \mathbf{H} \cdot \mathbf{H} \nabla \mu \mathrm{d}x \mathrm{d}y. \tag{53}$$

Since $\nabla \mu$ is zero for a homogeneous material, $\mathbf{f}^m$ is needed only to be integrated over a thin layer adjacent to the interface where μ changes from μ_s to μ_f while $\nabla \mu \to \infty$. Defining ∇ with respect to ξ and ζ, being coordinates normal and tangential to the interface, respectively, the magnetic field intensity becomes

$$\mathbf{H} = \frac{\partial \phi}{\partial \zeta} \mathbf{t} + \frac{\partial \phi}{\partial \xi} \mathbf{n}. \tag{54}$$

Therefore, Eq. (53) can be rewritten as

$$\mathbf{F}_s^m = -\frac{1}{2} \int \int_{\Omega_s} \left[\left(\frac{\partial \phi}{\partial \zeta} \right)^2 + \left(\frac{\partial \phi}{\partial \xi} \right)^2 \right] \nabla \mu \mathrm{d}\xi \mathrm{d}\zeta. \tag{55}$$

The boundary conditions (8) and (9) imply that $\frac{\partial \phi}{\partial \xi}$ is discontinuous across the interface while the magnetic flux density normal to the interface, $\mu \frac{\partial \phi}{\partial \xi}$, is a continuous quantity. Also, since ϕ is

37

continuous at the interface, $\frac{\partial \phi}{\partial \zeta}$ is continuous across the interface. Using these facts, Eq. (55) can be integrated across the assumed thin layer in the normal direction

$$\mathbf{F}_s^m = -\frac{1}{2} \int_{\partial\Omega_s} \left[(\mu_f - \mu_s) \left(\frac{\partial \phi}{\partial \zeta} \right)^2 + \left(\frac{1}{\mu_s} - \frac{1}{\mu_f} \right) \left(\mu \frac{\partial \phi}{\partial \xi} \right)^2 \right] \mathbf{n} d\zeta. \tag{56}$$

The magnetic force per unit length, $\hat{\mathbf{f}}_s^m$, as introduced in Eq. (33) is the integrand of Eq. (56). The integral in Eq. (56) is numerically approximated as presented in Eq. (34).

Appendix II - Numerical Algorithm

A pseudo-code of the proposed solution algorithm is shown in Table 3.

Table 3: Summary of the proposed algorithm.

---

for each time-step n **do**
  find neighbouring particles;
  for each particle i **do**
    compute $\mathbf{C}_i$ and $\hat{\mathbf{C}}_i$ using Eqs. (19) and (23);
  end for
  for each particle i **do**
    compute spatial derivative operators (24) and (25);
  end for
  start *magnetic solver*
    construct the linear system of equations for ϕ using Eqs. (11) and (13);
    solve the linear system of equations for ϕ (using the BiCG-stab method);
    for each solid body s **do**
      calculate $\mathbf{F}_s^m$ using Eq. (34);
      calculate $\mathbf{M}_s^m$ using Eq. (35);
    end for
  end *magnetic solver*
  start *hydrodynamic solver*
    for each particle i **do**
      compute $\mathbf{v}_i^* = \mathbf{v}_i^n + dt \left(-\left\langle \frac{\nabla p}{\rho} \right\rangle_i^n + \left\langle \frac{\eta}{\rho} \nabla^2 \mathbf{v} \right\rangle_i^n \right)$;
    end for
    for each solid body s **do**
      compute $\mathbf{v}_s^*$ and $\mathbf{\Omega}_s^*$ using Eqs. (28) and (29);
      update acceleration and velocity of the boundary particles of solid body s;
    end for
    for each particle i **do**
      if i is positioned inside of the fluid domain **then**
        using $\mathbf{v}_i^*$ and p_i^n, compute ρ_i^*;
      end if
    end for
  Continued on the Next Page. . .

Table 3 – Continued

for each particle i **do**
  if i is positioned inside of the fluid domain **then**
    compute p_i^* using the equation of state (3);
  else (i is on a fluid-solid interface)
    calculate p_i^* due to boundary condition (4);
    compute ρ_i^* using the equation of state (3);
  end if
end for
for each particle i **do**
  compute $\mathbf{v}_i^{**} = \mathbf{v}_i^n + dt \left(-\left\langle \frac{\nabla p}{\rho} \right\rangle_i^* + \left\langle \frac{\eta}{\rho} \nabla^2 \mathbf{v} \right\rangle_i^* \right)$;
end for
for each solid body s **do**
  compute $\mathbf{v}_s^{**}$ and $\mathbf{\Omega}_s^{**}$ using Eqs. (28) and (29);
  update acceleration and velocity of the boundary particles of solid body s;
end for
for each particle i **do**
  if i is positioned inside of the fluid domain **then**
    using $\mathbf{v}_i^{**}$ and p_i^*, compute ρ_i^{**};
  end if
end for
for each particle i **do**
  if i is positioned inside of the fluid domain **then**
    compute p_i^{**} using the equation of state (3);
  else (i is on a fluid-solid interface)
    calculate p_i^{**} due to boundary condition (4);
    compute ρ_i^{**} using the equation of state (3);
  end if
end for
for each particle i **do**
  evaluate new field variables using $V_i^{n+1} = \frac{V_i^{**} + V_i^*}{2}$;
  if i is an internal particle **then**
    compute $\mathbf{r}_i^{n+1}$;
  end if
end for
for each solid body s **do**
  evaluate $\mathbf{v}_s^{n+1} = \frac{\mathbf{v}_s^{**} + \mathbf{v}_s^*}{2}$ and $\mathbf{\Omega}_s^{n+1} = \frac{\mathbf{\Omega}_s^{**} + \mathbf{\Omega}_s^*}{2}$;
  compute $\mathbf{r}_s^{n+1}$;
  update position of the boundary particles of solid body s with rigid body constraint;
end for
for each particle i **do**
  if i is positioned inside of the fluid domain **then**
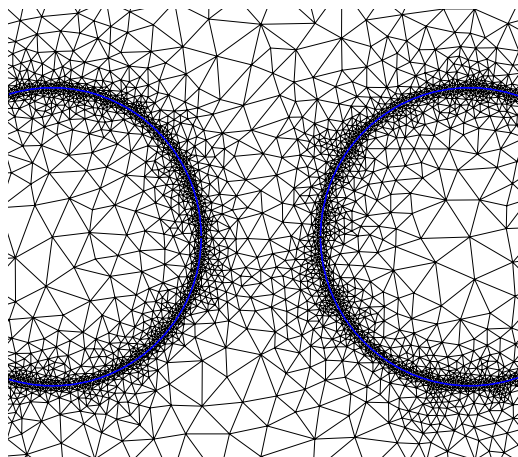   shift i using Eq. (39);
    update field variables;
Continued on the Next Page...

39

Figure 36: The finite element mesh generated around solid bodies for the case with $Gap = 0.001(m)$.

Table 3 – Continued

end if
end for
end *hydrodynamic solver*
end for

Appendix III - The Finite Element Method

As discussed earlier in this paper, the FEMM package [40] is utilized in order to obtain reference solutions for magnetostatic problems solved in Section 4.1. In this appendix, the procedure is elaborated. The whole domain is discretized using a boundary-fitted adaptive mesh with triangular elements. Convergent solutions for different cases, were obtained with almost 8000 elements. Figure 36 illustrates a portion of the grid used for the case with $Gap = 0.001(m)$.

The magnetostatic solver implemented in the FEMM package benefits from a formulation based on the vector potential function $\mathbf{A}$ where $\mathbf{B} = \nabla \times \mathbf{A}$. It can be shown that in a two-dimensional case without a free current, the Maxwell equations (5) and (6) combined with the corresponding boundary conditions (9) and (8) are reduced to an elliptic partial differential equation for $A = |\mathbf{A}|$. The resulting linear system of equations is solved using a preconditioned conjugate gradient solver. Once A is obtained, $\mathbf{B}$ can be calculated. For more information about the method see [40, 55]. The net magnetic force acting on a solid body is calculated by integrating the magnetic force density $\mathbf{f}_m = \nabla \cdot \mathbf{T_m}$ over the elements enclosed by the solid surface.

References

[1] T. G. Kang, M. A. Hulsen, P. D. Anderson, J. M. den Toonder, H. E. Meijer, Chaotic mixing induced by a magnetic chain in a rotating magnetic field, Physical Review E 76 (6) (2007) 066303.

[2] M. Zborowski, J. J. Chalmers, Magnetic cell separation, Vol. 32, Elsevier, 2011.

[3] N. Wereley, Magnetorheology: Advances and Applications, Vol. 6, Royal Society of Chemistry, 2013.

[4] Q. A. Pankhurst, J. Connolly, S. Jones, J. Dobson, Applications of magnetic nanoparticles in biomedicine, Journal of physics D: Applied physics 36 (13) (2003) R167.

[5] H. Suzuki, C.-M. Ho, N. Kasagi, A chaotic mixer for magnetic bead-based micro cell sorter, Microelectromechanical Systems, Journal of 13 (5) (2004) 779–790.

[6] D. J. Klingenberg, Magnetorheology: applications and challenges, AIChE Journal 47 (2) (2001) 246–249.

[7] G. Bossis, O. Volkova, S. Lacis, A. Meunier, Magnetorheology: fluids, structures and rheology, in: Ferrofluids, Springer, 2002, pp. 202–230.

[8] J. Ramos, D. Klingenberg, R. Hidalgo-Alvarez, J. de Vicente, Steady shear magnetorheology of inverse ferrofluids, Journal of Rheology 55 (1) (2011) 127–152.

[9] J. de Vicente, M. T. López-López, J. D. Durán, F. González-Caballero, Shear flow behavior of confined magnetorheological fluids at low magnetic field strengths, Rheologica acta 44 (1) (2004) 94–103.

[10] M. Mohebi, N. Jamasbi, J. Liu, Simulation of the formation of nonequilibrium structures in magnetorheological fluids subject to an external magnetic field, Physical Review E 54 (5) (1996) 5407.

[11] E. Climent, M. R. Maxey, G. E. Karniadakis, Dynamics of self-assembled chaining in magnetorheological fluids, Langmuir 20 (2) (2004) 507–513.

[12] R. Haghgooie, P. S. Doyle, Structure and dynamics of repulsive magnetorheological colloids in two-dimensional channels, Physical Review E 72 (1) (2005) 011405.

[13] S. Krishnamurthy, A. Yadav, P. Phelan, R. Calhoun, A. Vuppu, A. Garcia, M. Hayes, Dynamics of rotating paramagnetic particle chains simulated by particle dynamics, Stokesian dynamics and lattice Boltzmann methods, Microfluidics and Nanofluidics 5 (1) (2008) 33–41.

[14] J. F. Brady, G. Bossis, Stokesian dynamics, Annual review of fluid mechanics 20 (1988) 111–157.

[15] R. Bonnecaze, J. Brady, Dynamic simulation of an electrorheological fluid, The Journal of chemical physics 96 (3) (1992) 2183–2202.

[16] Y. Gao, M. Hulsen, T. Kang, J. den Toonder, Numerical and experimental study of a rotating magnetic particle chain in a viscous fluid, Physical Review E 86 (4) (2012) 041503.

[17] E. E. Keaveny, M. R. Maxey, Modeling the magnetic interactions between paramagnetic beads in magnetorheological fluids, Journal of Computational Physics 227 (22) (2008) 9554–9571.

[18] H. Ly, F. Reitich, M. Jolly, H. Banks, K. Ito, Simulations of particle dynamics in magnetorheological fluids, Journal of Computational Physics 155 (1) (1999) 160–177.

[19] Y. K. Suh, S. Kang, Motion of paramagnetic particles in a viscous fluid under a uniform magnetic field: benchmark solutions, Journal of Engineering Mathematics 69 (1) (2011) 25–58.

[20] T. G. Kang, Y. Gao, M. A. Hulsen, J. M. den Toonder, P. D. Anderson, Direct simulation of the dynamics of two spherical particles actuated magnetically in a viscous fluid, Computers & Fluids 86 (2013) 569–581.

[21] T. G. Kang, M. A. Hulsen, J. M. den Toonder, P. D. Anderson, H. E. Meijer, A direct simulation method for flows with suspended paramagnetic particles, Journal of Computational Physics 227 (9) (2008) 4441–4458.

[22] S. Kang, Y. Suh, An immersed-boundary finite-volume method for direct simulation of flows with suspended paramagnetic particles, International Journal for Numerical Methods in Fluids 67 (1) (2011) 58–73.

[23] T. G. Kang, M. A. Hulsen, J. M. den Toonder, Dynamics of magnetic chains in a shear flow under the influence of a uniform magnetic field, Physics of Fluids 24 (4) (2012) 042001.

[24] X. Bian, S. Litvinov, R. Qian, M. Ellero, N. A. Adams, Multiscale modeling of particle in suspension with smoothed dissipative particle dynamics, Physics of Fluids 24 (1) (2012) 012002.

[25] M. R. Hashemi, R. Fatehi, M. T. Manzari, A modified SPH method for simulating motion of rigid bodies in Newtonian fluid flows, International Journal of Non-Linear Mechanics 47 (6) (2012) 626–638.

[26] B. Vaughan, B. Smith, D. Chopp, A comparison of the extended finite element method with the immersed interface method for elliptic equations with discontinuous coefficients and singular sources, Communications in Applied Mathematics and Computational Science 1 (1) (2007) 207–228.

[27] J. A. Stratton, Electromagnetic theory, John Wiley & Sons, 1941.

[28] R. Fatehi, M. T. Manzari, Error estimation in smoothed particle hydrodynamics and a new scheme for second derivatives, Computers & Mathematics with Applications 61 (2) (2011) 482–498.

[29] R. Fatehi, M. T. Manzari, A consistent and fast weakly compressible smoothed particle hydrodynamics with a new wall boundary condition, International Journal for Numerical Methods in Fluids 68 (7) (2012) 905–921.

[30] W. Li, G. Chen, S. Yeo, Viscoelastic properties of MR fluids, Smart Materials and Structures 8 (4) (1999) 460.

[31] J. P. Morris, P. J. Fox, Y. Zhu, Modeling low Reynolds number incompressible flows using SPH, Journal of computational physics 136 (1) (1997) 214–226.

[32] M. Ellero, N. Adams, SPH simulations of flow around a periodic array of cylinders confined in a channel, International Journal for Numerical Methods in Engineering 86 (8) (2011) 1027–1040.

[33] J. D. Jackson, Classical electrodynamics, Wiley, New York, 1962.

[34] D. C. Jiles, Introduction to magnetism and magnetic materials, CRC Press, 1998.

[35] J. J. Monaghan, Smoothed particle hydrodynamics, Annual review of astronomy and astrophysics 30 (1992) 543–574.

[36] P. Randles, L. Libersky, Smoothed particle hydrodynamics: some recent improvements and applications, Computer methods in applied mechanics and engineering 139 (1) (1996) 375–408.

[37] X. Bian, M. Ellero, A splitting integration scheme for the SPH simulation of concentrated particle suspensions, Computer Physics Communications 185 (1) (2014) 53–62.

[38] Seldon C++ library for linear algebra, `http://seldon.sourceforge.net`, version 5.2 (2013).

[39] R. Xu, P. Stansby, D. Laurence, Accuracy and stability in incompressible SPH (ISPH) based on the projection method and a new approach, Journal of Computational Physics 228 (18) (2009) 6703–6725.

[40] D. Meeker, Finite element method magnetics, version 4.2 (2013).

[41] J. P. Morris, A study of the stability properties of SPH, arXiv preprint astro-ph/9503124.

[42] N. Lanson, J.-P. Vila, Renormalized meshfree schemes i: consistency, stability, and hybrid methods for conservation laws, SIAM Journal on Numerical Analysis 46 (4) (2008) 1912–1934.

[43] D. J. Price, Smoothed particle hydrodynamics and magnetohydrodynamics, Journal of Computational Physics 231 (3) (2012) 759–794.

[44] A. K. Vuppu, A. A. Garcia, M. A. Hayes, Video microscopy of dynamically aggregated paramagnetic particle chains in an applied rotating magnetic field, Langmuir 19 (21) (2003) 8646–8653.

[45] S. Melle, O. G. Calderón, M. A. Rubio, G. G. Fuller, Microstructure evolution in magnetorheological suspensions governed by mason number, Physical Review E 68 (4) (2003) 041503.

[46] W. Coffey, Y. P. Kalmykov, Inertial effects in the complex magnetic susceptibility of a ferrofluid in the presence of a dc bias field, Journal of magnetism and magnetic materials 164 (1) (1996) 133–142.

[47] D. J. Klingenberg, J. C. Ulicny, M. A. Golden, Mason numbers for magnetorheology, Journal of Rheology 51 (5) (2007) 883–893.

[48] W. H. Li, H. Du, G. Chen, S. H. Yeo, N. Guo, Nonlinear viscoelastic properties of MR fluids under large-amplitude-oscillatory-shear, Rheologica acta 42 (3) (2003) 280–286.

[49] J. D. Ferry, Viscoelastic properties of polymers, John Wiley & Sons, Inc, 1980.

[50] A. C. Pipkin, Lectures on viscoelasticity theory, Springer-Verlag, New York, 1972.

[51] M. Toivakka, D. Eklund, D. W. Bousfield, Prediction of suspension viscoelasticity through particle motion modeling, Journal of non-Newtonian fluid mechanics 56 (1) (1995) 49–64.

[52] J. L. Schrag, Deviation of velocity gradient profiles from the gap loading and surface loading limits in dynamic simple shear experiments, Transactions of The Society of Rheology 21 (3) (1977) 399–413.

[53] F. Ding, A. Jeffrey Giacomin, R. Byron Bird, C.-B. Kweon, Viscous dissipation with fluid inertia in oscillatory shear flow, Journal of non-Newtonian fluid mechanics 86 (3) (1999) 359–374.

[54] R. H. Ewoldt, A. Hosoi, G. H. McKinley, New measures for characterizing nonlinear viscoelasticity in large amplitude oscillatory shear, Journal of Rheology 52 (6) (2008) 1427–1458.

[55] P. P. Silvester, R. L. Ferrari, Finite elements for electrical engineers, Cambridge university press, 1996.